Acta Mech 225, 2319–2343 (2014)
DOI 10.1007/s00707-014-1155-8

N. Kumar · S. Luding · V. Magnanimo

Macroscopic model with anisotropy based on micro–macro information

Received: 25 April 2013 / Revised: 2 July 2014 / Published online: 26 July 2014

Abstract Physical experiments can characterize the elastic response of granular materials in terms of macroscopic state variables, namely volume (packing) fraction and stress, while the microstructure is not accessible and thus neglected. Here, by means of numerical simulations, we analyze dense, frictionless granular assemblies with the final goal to relate the elastic moduli to the fabric state, i.e., to microstructural averaged contact network features as contact number density and anisotropy. The particle samples are first isotropically compressed and then quasi-statically sheared under constant volume (undrained conditions). From various static, relaxed configurations at different shear strains, infinitesimal strain steps are applied to "measure" the effective elastic response; we quantify the strain needed so that no contact and structure rearrangements, i.e. plasticity, happen. Because of the anisotropy induced by shear, volumetric and deviatoric stresses and strains are cross-coupled via a single anisotropy modulus, which is proportional to the product of deviatoric fabric and bulk modulus (i.e., the isotropic fabric). Interestingly, the shear modulus of the material depends also on the actual deviatoric stress state, along with the contact configuration anisotropy. Finally, a constitutive model based on incremental evolution equations for stress and fabric is introduced. By using the previously measured dependence of the stiffness tensor (elastic moduli) on the microstructure, the theory is able to predict with good agreement the evolution of pressure, shear stress and deviatoric fabric (anisotropy) for an independent undrained cyclic shear test, including the response to reversal of strain.

1 Introduction

Granular materials behave differently from usual solids or fluids and show peculiar mechanical properties like dilatancy, history dependence, ratcheting and anisotropy [24,25,28,30,39,40,60,70,75,76,87]. The behavior of these materials is highly nonlinear and involves plasticity also for very small strain due to rearrangements of the elementary particles [4,15,22]. The concept of an initial purely elastic regime (small strain) for granular assemblies is an issue still under debate in the mechanical and geotechnical communities. On the other hand, approaches that neglect the effect of elastic stored energy are also questionable, i.e., all the work done by the internal forces is dissipated. Features visible in experiments, like wave propagation, can hardly be described without considering an elastic regime. In a general picture, both the deformations at contact and the irrecoverable rearrangements of the grains sum up to the total strain. The former represents the elastic, reversible contribution to the behavior of the material. That is, for very small strain, the response of a finite granular system in static equilibrium can be assumed to be linearly elastic [20,42,59,70], as long as no irreversible rearrangements take place.

Presented at the 8th European Solid Mechanics Conference in the Graz University of Technology, Austria, 9–13 July 2012.

N. Kumar (✉) · S. Luding · V. Magnanimo
Multi Scale Mechanics (MSM), Faculty of Engineering Technology, MESA+,
University of Twente, P.O. Box 217, 7500 AE Enschede, The Netherlands
E-mail: n.kumar@utwente.nl

Despite these arguments and the long-standing debate, basic features of the physics of granular elasticity are currently unresolved, like the determination of a proper set of state variables to describe the effective moduli. Physical experiments carried out on sand and glass beads show that wave propagation in the aggregate depends upon the stress state and the volume fraction [19,32,36,42,80,83]. Recent works [1,28,36,43,87] show that along with the macroscopic properties (stress and volume fraction) [19,36,86], also the fabric [10,47,61,70,87] plays a crucial role, as it characterizes, on average, the geometric arrangement of contacts. Due to preparation and loading path, the microstructure of granular aggregates is often far from isotropic, and this is at the origin of interesting features in those materials. The mechanical behavior of anisotropic soils is a topic of current interest for both experimental and theoretical investigations. As one example, extensive experimental work on anisotropy has been carried out on laboratory-prepared (by careful "raining" or bedding) sand specimens [81,84]. These and other studies show that the sample deformation characteristics depends highly on the orientation of the bedding plane with respect to the principal stress and strain axes [19,43,61,82–84]. On the other hand, when the material is sheared, anisotropy in the contact network develops, as related to the opening and closing of contacts, restructuring, and the creation and destruction of force-chains, affecting the material response [3,42,77,80,87].

Most standard constitutive models, involving elasticity and/or plasticity have been applied to describe the incremental behavior of (an)isotropic granular solids—sometimes with success, but typically only in a limited range of parameters. In the majority of the models, the stress increment is related to the actual stress state of the granular system and its density. This is the case for hypoplasticity [23,36], where a single nonlinear tensorial equation relates the Jaumann stress-rate with strain-rate and stress tensors. Only few theories after the pioneer work by Cowin [12] consider explicitly the influence of the micro-mechanic structure on the elastic stiffness, plastic flow rule or non-coaxiality of stress and strain, see [7,8,13,57,58,75,76] and references therein. The evolution of microstructure due to deformations is an essential part of a constitutive model for granular matter because it stores the information how different paths have affected the mechanical state of the system. In this sense, fabric is a tensorial history variable. When included in the formulation, the effect of structure is often described by a fixed fabric tensor normal to the bedding plane of deposited sands [13,45,76,81]. Recently, Li and Dafalias [46] have proposed a new framework (rather than a specific constitutive model) by reconsidering the classical steady state theory by Roscoe et al. [67], with a fabric tensor evolving towards a properly defined steady state value. This is supported by experimental [84] and extensive numerical works [28,30,47,77,87]. In a similar fashion, the anisotropy model proposed in [48,51] postulates the split of isotropic and deviatoric stress, strain and fabric and includes the microstructure as a state variable, whose behavior is described by an evolution equation independent of stress. References [30,39] predict uniaxial simulation results under this assumption (the evolutions of stress and structure are independent from each other), where the simplified model captures well the qualitative behavior.

In this work, we use the discrete element method (DEM) to study granular assemblies made of polydisperse frictionless particles and focus on their elastic behavior. By isolating elasticity, we aim to distinguish the kinematics at the microscale that lead to either macroscopic elasticity or plasticity. We analyze the role of microstructure, stress state and volume fraction on the evolution of the elastic moduli, with the goal to characterize them in terms of a unique, limited set of variables. In order to calculate the stiffness tensor, we apply small strain probes to various equilibrium states along a volume-conserving (undrained) shear deformation path. In the case of a finite assembly of particles, in simulations, an elastic regime can always be detected, and the elastic stiffnesses can be measured by means of an actual, very small, strain perturbation [50]. The purpose is to improve the understanding of elasticity in particle systems and to guide further developments for new constitutive models. As an example, the relation between moduli and fabric here is used in the anisotropic constitutive model, as proposed in [48,51], to predict the macroscopic behavior during a more general deformation path, involving also strain reversal.

This paper is organized as follows: The simulation method and parameters used and the averaging definitions for scalar and tensorial quantities are given in Sect. 2. The preparation test procedures and the results from the deviatoric simulation are explained in Sect. 3. Section 4 is devoted to the measurement of elastic moduli by means of small isotropic and deviatoric perturbations. There we present the evolution of the moduli with strain and link them to fabric and stress. Finally, in Sect. 5, theoretically, the evolution of the microstructural anisotropy is related to that of stress and strain, as proposed in Refs. [48,51]. This displays the predictive quality of the model, calibrated only for isochoric, unidirectional shear, when applied to an independent, cyclic shear test.

2 Numerical simulation

The Discrete Element Method (DEM) [2,30,47] helps to study the deformation behavior of particle systems. At the basis of DEM are laws that relate the interaction force to the overlap (relative deformation) of two particles. Neglecting tangential forces, if all normal forces $\mathbf{f}_i$ acting on particle i, from all sources, are known, the problem is reduced to the integration of Newton's equations of motion for the translational degrees of freedom:

$$\frac{\mathrm{d}}{\mathrm{d}t}\left(m_i \mathbf{v}_i\right) = \mathbf{f}_i + m_i \mathbf{g}, \tag{1}$$

with the mass m_i of particle i, its position $\mathbf{r}_i$, velocity $\mathbf{v}_i$ ($=\dot{\mathbf{r}}_i$) and the resultant force $\mathbf{f}_i = \sum_c \mathbf{f}_i{}^c$ acting on it due to contacts with other particles or with the walls, and the acceleration due to gravity, $\mathbf{g}$ (which is neglected in this study). The force on particle i, from particle j, at contact c, has normal and tangential components, but the latter are disregarded in this study to focus on frictionless packings.

For the sake of simplicity, the linear visco-elastic contact model for the normal component of force is used,

$$f^n = k\delta + \gamma\dot{\delta}, \tag{2}$$

where k is the spring stiffness, γ is the contact viscosity parameter, $\delta = \left(d_i + d_j\right)/2 - \left(\mathbf{r}_i - \mathbf{r}_j\right)\cdot\hat{\mathbf{n}}$ is the overlap between two interacting species i and j with diameters d_i and d_j, $\hat{\mathbf{n}} = \left(\mathbf{r}_i - \mathbf{r}_j\right)/\left|\left(\mathbf{r}_i - \mathbf{r}_j\right)\right|$ and $\dot{\delta}$ is the relative velocity in the normal direction. In order to reduce dynamical effects and shorten relaxation times, an artificial viscous background dissipation force $\mathbf{f}_b = -\gamma_b \mathbf{v}_i$ proportional to the moving velocity $\mathbf{v}_i$ of particle i is added, resembling the damping due to a background medium, as e.g., a fluid.

The standard simulation parameters are $N = 9{,}261 (=21^3)$ particles with average radius $\langle r\rangle = 1$ (mm), density $\rho = 2{,}000\,(\mathrm{kg/m^3})$, elastic stiffness $k = 10^8\,(\mathrm{kg/s^2})$, particle damping coefficient $\gamma = 1$ (kg/s), background dissipation $\gamma_b = 0.1$ (kg/s). Note that the polydispersity of the system is quantified by the width ($w = r_{\max}/r_{\min} = 3$) of a uniform size distribution [24], where $r_{\max}$ and $r_{\min}$ are the radii of the biggest and smallest particles, respectively.

The average time scale is determined when two averaged size particles (with $r_{\mathrm{avg}} = \langle r\rangle = 1$) with mass $m_{\mathrm{avg}} = \rho\left(4\pi r_{\mathrm{avg}}^3/3\right) = 8.377\,(\mu\mathrm{g})$ interact and is given as $t_{c,\mathrm{avg}} = \pi/\sqrt{k/m'_{\mathrm{avg}} - \left(\gamma/\left(2m'_{\mathrm{avg}}\right)\right)^2} = 0.6431\,(\mu\mathrm{s})$, where $m'_{\mathrm{avg}} = m_{\mathrm{avg}}/2$ is the reduced mass, with restitution coefficient $e_{\mathrm{avg}} = \exp\left(-\gamma t_{c,\mathrm{avg}}/\left(2m'_{\mathrm{avg}}\right)\right) = 0.926$. The fastest response time scale in the system is determined when two smallest particle with mass $m_{\mathrm{small}} = \rho\left(4\pi r_{\min}^3/3\right) = 1.047\ (\mu\mathrm{g})$ interact, and is given as $t_{c,\mathrm{small}} = \pi/\sqrt{k/m'_{\mathrm{small}} - \left(\gamma/\left(2m'_{\mathrm{small}}\right)\right)^2} = 0.2279\ (\mu\mathrm{s})$, where $m'_{\mathrm{small}} = m_{\mathrm{small}}/2$ is the reduced mass, with restitution coefficient $e_{\mathrm{small}} = \exp\left(-\gamma t_{c,\mathrm{small}}/\left(2m'_{\mathrm{small}}\right)\right) = 0.804$.

2.1 Coordination number and fraction of rattlers

In order to link the macroscopic load carried by the sample with the active microscopic contact network, all particles that do not contribute to the force network are excluded. Frictionless particles with <4 contacts are thus "rattlers," since they cannot be mechanically stable and hence do not contribute to the contact or force network [24,30,39]. The classical definition of coordination number is $C = M/N$, where M is the total numbers of contacts and $N = 9{,}261$ is the total number of particles. The corrected coordination number is: $C^* = M_4/N_4$, where, M_4 is the total number of contacts of the N_4 particles with at least four contacts. Moreover, we introduce here the reduced number of contacts M_4^p, where contacts related to rattlers are excluded twice, as they do not contribute to the stability of both the rattler and the particle in contact with it. Hence, $M_4^p = M_4 - M_1 - M_2 - M_3 = M - 2\left(M_1 + M_2 + M_3\right)$, where M_1, M_2 and M_3 are total numbers of contacts of particles with only 1, 2 and 3 contacts, respectively. This leads to a modification in the definition of the corrected coordination number: $C_p^* = M_4^p/N_4$. The fraction of rattlers is $\phi_r = \left(N - N_4\right)/N$; hence, $C = C^*\left(1 - \phi_r\right)$. The total volume of particles is $\sum_{\mathcal{P}=1}^{N} V_{\mathcal{P}} = (4/3)\pi N\langle r^3\rangle$, where $\langle r^3\rangle$ is the third moment of the size distribution [24,39], and the volume fraction is defined as $\nu = (1/V)\sum_{\mathcal{P}=1}^{N} V_{\mathcal{P}}$, where V is the volume of the periodic system.

2.2 Macroscopic (tensorial) quantities

Here, we focus on defining averaged tensorial macroscopic quantities—including strain-, stress- and fabric (structure) tensors—that provide information about the state of the packing and reveal interesting bulk features.

By speaking about the strain-rate tensor $\dot{\mathbf{E}}$, we refer to the external strain that we apply to the sample in a time interval dt. The isotropic part of the infinitesimal strain tensor ε_{v} [24,30,39] is defined as:

$$\delta\varepsilon_{\mathrm{v}} = -\dot{\varepsilon}_{\mathrm{v}}\mathrm{d}t = -\frac{\delta\varepsilon_{xx} + \delta\varepsilon_{yy} + \delta\varepsilon_{zz}}{3} = -\frac{1}{3}\mathrm{tr}(\delta\mathbf{E}) = -\frac{1}{3}\mathrm{tr}(\dot{\mathbf{E}})\mathrm{d}t \tag{3}$$

where $\varepsilon_{\alpha\alpha} = \dot{\varepsilon}_{\alpha\alpha}\mathrm{d}t$ with $\alpha\alpha = xx, yy$ and zz are the diagonal components of the tensor in the Cartesian $x - y - z$ reference system. The trace integral of $3\varepsilon_{\mathrm{v}}$ is denoted as the volumetric strain ε_v, the true or logarithmic strain, i.e., the volume change of the system, relative to the initial reference volume, V_0.

On the other hand, from DEM simulations, one can measure the "static" stress in the system [9] as

$$\boldsymbol{\sigma} = (1/V)\sum_{c\in V}\mathbf{l}^c \otimes \mathbf{f}^c, \tag{4}$$

averaged over all the contacts in the volume V of the dyadic products between the contact force $\mathbf{f}^c$ and the branch vector $\mathbf{l}^c$, where the contribution of the kinetic fluctuation energy has been neglected [30,47]. The isotropic component of the stress is the pressure $P = \mathrm{tr}(\boldsymbol{\sigma})/3$.

In order to characterize the geometry/structure of the static aggregate at microscopic level, we will measure the fabric tensor, defined as

$$\mathbf{F} = \frac{1}{V}\sum_{\mathcal{P}\in V} V^{\mathcal{P}} \sum_{c\in\mathcal{P}} \mathbf{n}^c \otimes \mathbf{n}^c \tag{5}$$

where $V^{\mathcal{P}}$ is the volume of particles $\mathcal{P}$, which lie inside the averaging volume V, and $\mathbf{n}^c$ is the normal unit branch vector pointing from center of particle $\mathcal{P}$ to contact c [40,47,86]. We want to highlight that a different convention for the fabric tensor involves only the orientation of contacts as follows [61,69,87]:

$$\mathbf{F}^o = \frac{1}{N_c}\sum_{c\in N_c} \mathbf{n}^c \otimes \mathbf{n}^c \tag{6}$$

where N_c is the total number of contacts in the system. An approximated relationship between Eqs. (5) and (6) can be derived as:

$$\mathbf{F}^o \approx \frac{3\mathbf{F}}{\mathrm{tr}(\mathbf{F})}, \tag{7}$$

with $\mathrm{tr}(\mathbf{F}^o) = 1$. This relation is exactly equal for monodisperse assemblies but largely deviates for assemblies with high polydispersity (see further discussion in Sect. 3). The difference also becomes more significant when the jamming volume fraction [52,79] is approached. In the following, when not explicitly stated, we will refer to Eq. (5), since we combine the effects of volume fraction and number/orientation of contacts, both relevant quantities when the elastic moduli are considered [24].

In a large volume with a given distribution of particle radii, the isotropic fabric, i.e., the trace of $\mathbf{F}$, is proportional to the volume fraction ν and the coordination number C, see Refs. [24,30,39], as

$$F_{\mathrm{v}} = \mathrm{tr}(\mathbf{F}) = g_3\nu C = g_3\nu C^*\left(1 - \phi_r\right), \tag{8}$$

where C, C^* and ϕ_r have been introduced in previous Sect. 2.1, and $g_3 \approx 1.22$ for polydispersity $w = 3$, being only a weighted factor of order unity of the non-dimensional moments size distribution [24,39,71].

2.3 Isotropic and deviatoric parts

We choose here to describe each symmetric second order tensor $\mathbf{Q}$, in terms of its isotropic part (first invariant) and the second,

$$J_2 = \frac{1}{2}\left[\left(Q_1^D\right)^2 + \left(Q_2^D\right)^2 + \left(Q_3^D\right)^2\right],$$

and third,

$$J_3 = \det(\mathbf{Q}^D) = Q_1^D Q_2^D Q_3^D,$$

invariants of the deviator, with Q_1^D, Q_2^D and Q_3^D eigenvalues of the deviatoric tensor $\mathbf{Q}^D = \mathbf{Q} - (\mathrm{tr}(\mathbf{Q})/3)\mathbf{I}$. We use the following definition (of the Euclidean or Frobenious norm) to quantify with a single scalar the magnitude of the deviatoric part [39,40] of $\mathbf{Q}$:

$$\begin{aligned} Q_{\mathrm{dev}} &= \mathrm{Fsgn}\,(\mathbf{Q})\sqrt{2J_2} \\ &= \mathrm{Fsgn}\,(\mathbf{Q})\sqrt{\frac{\left(Q_{xx}-Q_{yy}\right)^2+\left(Q_{yy}-Q_{zz}\right)^2+(Q_{zz}-Q_{zz})^2+6\left(Q_{xy}^2+Q_{yz}^2+Q_{zx}^2\right)}{3}}, \end{aligned} \tag{9}$$

where Q_{xx}, Q_{yy} and Q_{zz} are its diagonal, Q_{xy}, Q_{yz} and Q_{zx} its off-diagonal components and the deviators $\varepsilon_{\mathrm{dev}}$, σ_{dev} and F_{dev} refer to strain $\mathbf{E}$, stress $\boldsymbol{\sigma}$ and fabric $\mathbf{F}$, respectively. Fsgn $(\mathbf{Q})$ is the sign function that relates the tensorial quantity to be measured, $\mathbf{Q}$, with the reference tensor that describes the (strain- or stress-controlled) path applied to the sample, $\mathbf{H}_0$:

$$\mathrm{Fsgn}\,(\mathbf{Q}) = \mathrm{sgn}\,(\mathbf{H}_0 : \mathbf{Q}),$$

with ":" being the inner product between the two tensors. For a given, complex deformation path, the reference tensor $\mathbf{H}_0$ must be chosen in a convenient way, in order to take into account both the actual loading path and/or the previous deformation history of the sample. In the special case of an undrained shear test, as introduced later in Sect. 3, we use as reference the director of the strain-rate $\mathbf{H}_0 = \hat{D}(-\dot{\mathbf{E}}) \propto (-1, 1, 0)$, where only the diagonal terms are given (and the normalization can be ignored), see Eq. (10) below, so that Fsgn simplifies to

$$\mathrm{Fsgn}\,(\mathbf{Q}) = \mathrm{sgn}\left(Q_{yy} - Q_{xx}\right),$$

with x-wall expanding, y-wall compressing and z-wall non-mobile [39]. We want to point out here that, during a deformation, the response of stress $\boldsymbol{\sigma}$ and fabric $\mathbf{F}$ is opposite in sign to applied strain-rate $\dot{\mathbf{E}}$. Unless mentioned explicitly, we will be using a sign convention for strain (isotropic $\delta\varepsilon_{\mathrm{v}} = -(1/3)\mathrm{tr}(\delta\mathbf{E})$ and deviatoric $\delta\varepsilon_{\mathrm{dev}} = -\delta E_{\mathrm{dev}}$), such that consistently a positive strain increment leads to a positive stress and fabric response.

Finally we note that in this work we will use $k^* = k/(2\langle r\rangle)$ to non-dimensionalize pressure P and deviatoric stress σ_{dev} to give P^* and σ^*_{dev}, respectively, and will be referring to deviatoric stress as shear stress.[1]

3 Volume-conserving (undrained) biaxial shear test

In this section, we first describe the sample preparation procedure and then the details of the numerical shear test.

The initial configuration is such that spherical particles are randomly generated, with low volume fraction and rather large random velocities in a periodic 3D box, such that they have sufficient space and time to exchange places and to randomize themselves. This granular gas is then compressed isotropically, to a target volume fraction $\nu_0 = 0.640$, sightly below the isotropic jamming volume fraction [30,39,52] $\nu_c \approx 0.658$ and then relaxed to allow the particles to fully dissipate their potential energy [30,39].[2] The relaxed state is then compressed (loading) isotropically from ν_0 to a higher volume fraction of $\nu = 0.82$, and decompressed back (unloading) to ν_0 [30,39].

[1] It is important to point out that the rattlers are excluded in defining the (corrected) coordination number C^*. However, dynamic rattler particles with $1 \leq M_p \leq 3$ contacts are included in the definitions of fabric and stress. We verified that during shear deformation, the maximum contribution in deviatoric stress due to rattlers is 0.03 %, while in the case of deviatoric fabric the contribution can be as large as 0.5 %. This is not surprising since only contacting particles contribute to the definitions of both stress and fabric, and dynamic rattlers have a smaller weight for stress than for fabric, see Eq. (5). Note also that the number of rattlers decreases with increasing size of the particles [39].

[2] Note that the jamming volume fraction is given for a uniform radius distribution for polydispersity $w = 3$. The results will be different if the distribution is different, e.g., when uniform surface or volume distributions are used. See Ref. [39] for a detailed discussion on the evolution of jamming volume fractions with polydispersity for a uniform radius distribution.

The preparation procedure, as described above, provides many different initial configurations with volume fractions ν_i, each one in mechanical equilibrium. Starting from various ν_i chosen from the unloading branch [30,39], the samples are then sheared keeping the total volume constant, that is with a strain-rate tensor

$$\dot{\mathbf{E}} = \dot{\varepsilon}_{\mathrm{yy}} \begin{bmatrix} -1 & 0 & 0 \\ 0 & +1 & 0 \\ 0 & 0 & 0 \end{bmatrix} \tag{10}$$

where $\dot{\varepsilon}_{\mathrm{yy}} = 2.84\ 10^{-5}$ [s^{-1}] is the strain-rate (compression > 0) amplitude applied to the moving x- and y-walls, while the third z-wall is stationary. Our shear test, where the total volume is conserved during deformation, resembles an undrained test typical in geotechnical practice [87]. The chosen deviatoric path is on the one hand similar to the pure shear situation, and on the other hand allows for simulation of the biaxial element test [56,66] (with two walls static, while four walls are moving, in contrast to the more difficult isotropic compression, where all the six walls are moving). Pure shear is here used to identify constant volume deviatoric loading with principal strain axis keeping the same orientation as the geometry (cuboidal) of the system for the whole experiment. In this case, there is no rotation (vorticity) of the principal strain (rate) axis, and no distortion/rotation of the sample due to shear deformation. Different types of volume-conserving deviatoric deformations can be applied to shear the system, but very similar behavior has been observed [30], in terms of shear stress.

3.1 Evolution of stress

The evolution of non-dimensional pressure P^* with deviatoric strain $\varepsilon_{\mathrm{dev}}$ is presented in Fig. 1a during undrained shear tests for some exemplary volume fraction. For frictionless systems analyzed here, only a slight variation of the pressure is observed at the beginning of the test, due to the development of anisotropy in the sample, after which P^* remains constant.[3] Both the (small) initial pressure change and the final saturation value vary with the vicinity of ν to the jamming volume fraction ν_c. Interestingly, depending on the volume fraction, some of the samples show increase in the pressure (dilatancy) with respect to the initial value and some other decrease (compactancy), as shown in Fig. 1. This supports the idea of a certain threshold value $\nu_d^p = 0.79$, as shown in Fig. 2a, where the pressure of the system changes behavior, similarly to the switch between volumetric dilation and contraction visible in triaxial tests.

The evolution of the (non-dimensional) shear stress σ^*_{dev} during shear, as function of the deviatoric strain $\varepsilon_{\mathrm{dev}}$, is shown in Fig. 1b, for the same simulations as in Fig. 1a. The stress grows with applied strain until an asymptote (of maximum stress anisotropy) is reached where it remains fairly constant, with slight fluctuations around the maximum σ^*_{dev} [10]. The growth rate and the asymptote of σ^*_{dev}, both increase with ν.

3.2 Evolution of fabric

Complementary to stress, in this subsection we study the evolution of the microstructure in the sample during the volume-conserving shear test. Figure 3a shows that the isotropic fabric F_{v} behaves in a very similar fashion as P^*, with a slight increase/decrease at the beginning, followed by saturation stage, whose value increases continuously with ν. Figure 2b shows that the difference between the initial value of F_{v} and its saturation value changes sign when a certain volume fraction, $\nu_d^F = 0.755$, is reached. Note that $\nu_d^F \neq \nu_d^p$, that further confirms the independent evolution of $\boldsymbol{F}$ and $\boldsymbol{\sigma}$.

From Eq. (8) F_{v} is proportional to the product of volume fraction ν, that remains unchanged during deviatoric deformations, and coordination number C, that varies only slightly for sheared frictionless systems [30]. Note that as $C = C^*(1 - \phi_r)$, knowing the (empirical) relations of C^* and ϕ_r with volume fraction, as presented in Refs. [30,39], we can fully describe the isotropic fabric state. In this study, we assume F_{v} to stay constant during the shear test. This assumption will be used later in Sect. 5 for the prediction of a cyclic shear test. However, the small changes in F_{v} or P^* can be associated with a (small) change in the jamming volume fraction [41].

[3] We observe a much more pronounced change in pressure when friction is included in the calculation, in agreement with other studies, see e.g., [28]. These data are not shown here and are subject of ongoing research.

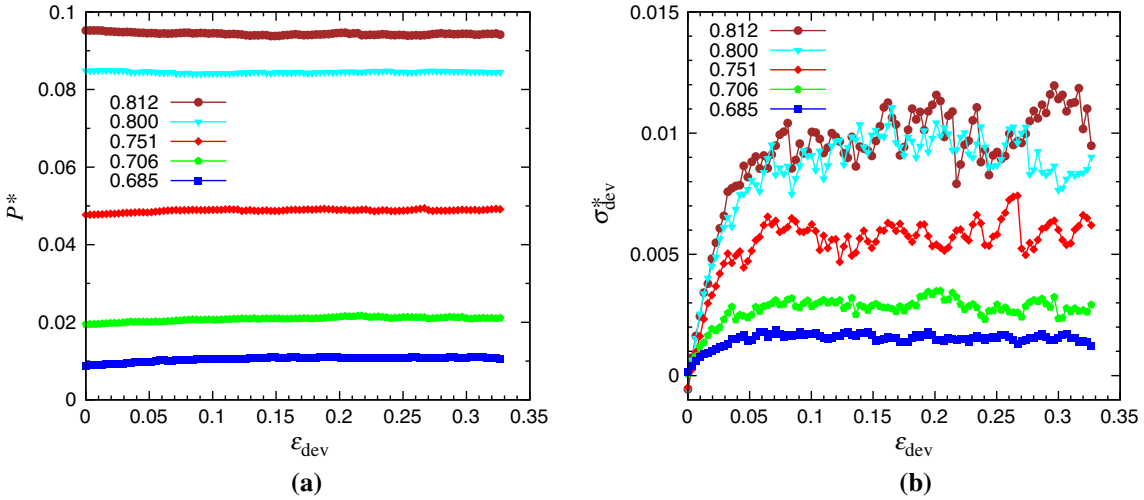

Fig. 1 Evolution of non-dimensional **a** pressure P^* and **b** shear stress $\sigma^*_{\rm dev}$ along the main strain path for the pure shear deformation mode for five different volume fractions, as given in the *inset* (color figure online)

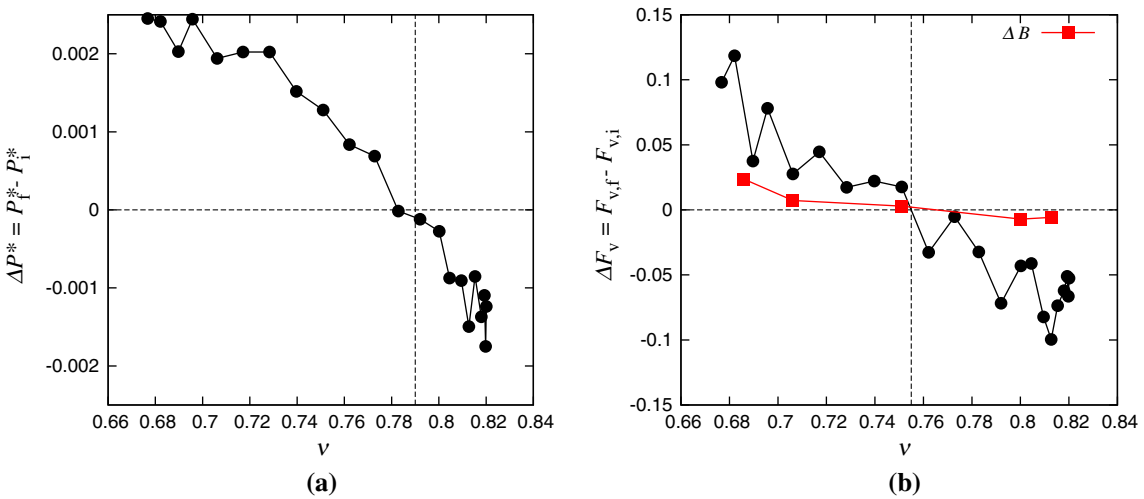

Fig. 2 Difference between the final and initial values in **a** non-dimensional pressure P^* and **b** isotropic fabric $F_{\rm v}$ for the pure shear deformation mode for different volume fractions. *Red squares* represent the change in bulk modulus, as derived in Sect. 4.3. *Dashed lines* in the *plots* represent the crossover when these quantities change sign (color figure online)

The evolution of the deviatoric fabric, $F_{\rm dev}$, as function of the deviatoric strain is shown in Fig. 3b during shear for five different volume fractions. It builds up from different random small initial values (due to the initial anisotropy in the sample that develops during preparation) and reaches different maxima. The deviatoric fabric builds up faster at lower volume fractions but the maximal values are higher for smaller volume fractions, qualitatively opposite to the evolution of $\sigma^*_{\rm dev}$ [10]. As mentioned in Sect. 2.2 the validity of Eq. (7), that relates the two different definitions of fabric, depends on polydispersity. In order to check the relation, in Fig. 4 the evolution of the three eigenvalues of the fabric tensor is plotted, for both definitions, Eqs. (5) and (6), during the volume-conserving shear test, for three different values of polydispersity $w = 1, 2$ and 3. For all polydispersities, the chosen volume fraction $\nu = 0.685$ is close to the jamming points, that slightly vary with w [39]. The difference between the definitions of fabric becomes higher for higher polydispersity $w = 3$, as in Eq. (6) the contribution of each particle is weighted by its surface area (via its number of contacts), whereas in Eq. (5) it is weighted by the volume. Only for the monodisperse case, the relation is exact, as can be seen in Fig. 4a. The differences are considerable for $w = 2$ and $w = 3$, for both compressive and tensile direction, while the non-mobile direction is not affected. Note that the difference of the two fabrics will be smaller for denser systems.

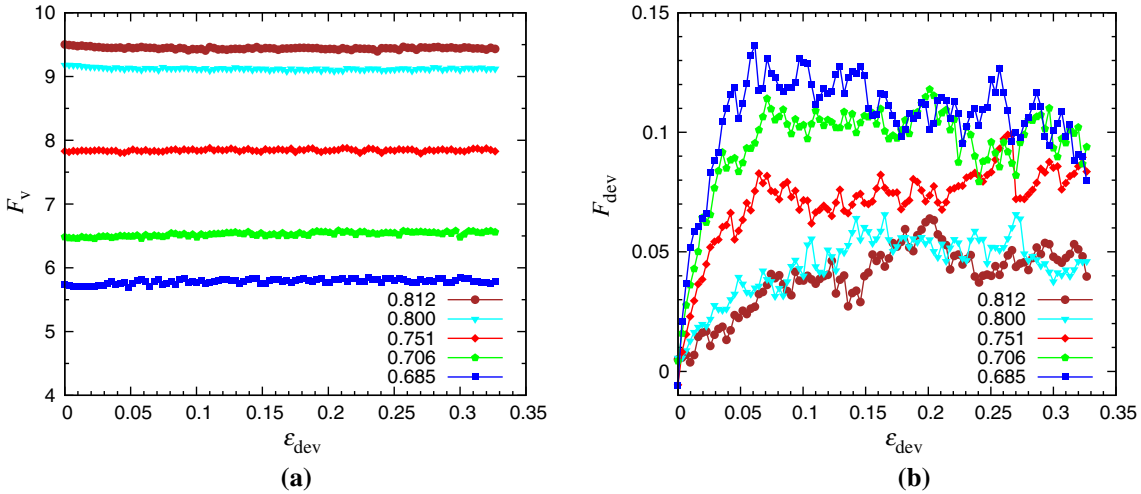

Fig. 3 Evolution of **a** isotropic fabric F_v and **b** deviatoric fabric F_{dev} along the main strain path for the pure shear deformation mode for five different volume fractions, as given in the *inset* (color figure online)

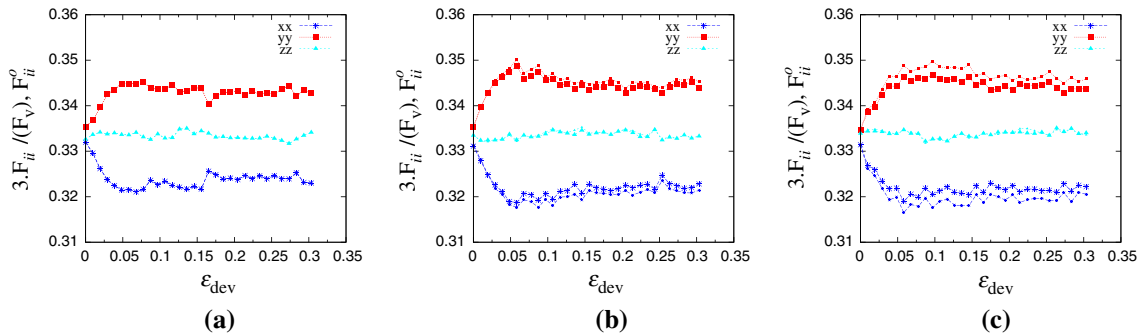

Fig. 4 Evolution of the eigen-values of the fabric tensors (directions shown in the *inset*), during shear deformation at volume fraction $\nu = 0.685$, for the fabric definition defined in Eq. (6) (*smaller symbols*) and the relation presented in Eq. (7) (*large symbols*), for three cases of polydispersity. **a** $w = 1$, i.e., monodisperse, **b** $w = 2$ and **c** $w = 3$ (present work) (color figure online)

4 Elastic moduli

In this section, we focus on the evolution of the elastic properties of the material and neglect the plastic contribution to the granular behavior that will be superimposed to the present analysis later in Sect. 5. We first describe the numerical procedure to measure the elastic moduli of the anisotropic aggregate, and later analyze the data and their relation with stress and fabric.

4.1 Numerical probes

In a general framework, a possible description for the incremental, elastic behavior of an anisotropic material is

$$\begin{bmatrix} \delta P^* \\ \delta \sigma^*_{dev} \end{bmatrix} = \begin{bmatrix} B & A_1 \\ A_2 & G^{oct} \end{bmatrix} \begin{bmatrix} 3\delta\varepsilon_v \\ \delta\varepsilon_{dev} \end{bmatrix}, \tag{11}$$

where the isotropic and deviatoric components of stress have been isolated and are expressed as functions of ε_v and ε_{dev} via a non-dimensional stiffness matrix [26] (by multiplying the moduli with k^*, the real stiffnesses can be extracted). B is the classical bulk modulus, and G^{oct} the octahedral shear modulus. The anisotropy moduli A_1 and A_2 provide a cross-coupling between the two parts (isotropic and deviatoric) of stress and strain increments. Equation (11) provides a partial description for the evolving stress and stiffness of a sheared material, as it applies to a triaxial-box configuration (with eigen-system coincident with the axes of the box), where no off-diagonal terms are measured and stress and moduli are assumed to be collinear. Moreover, the

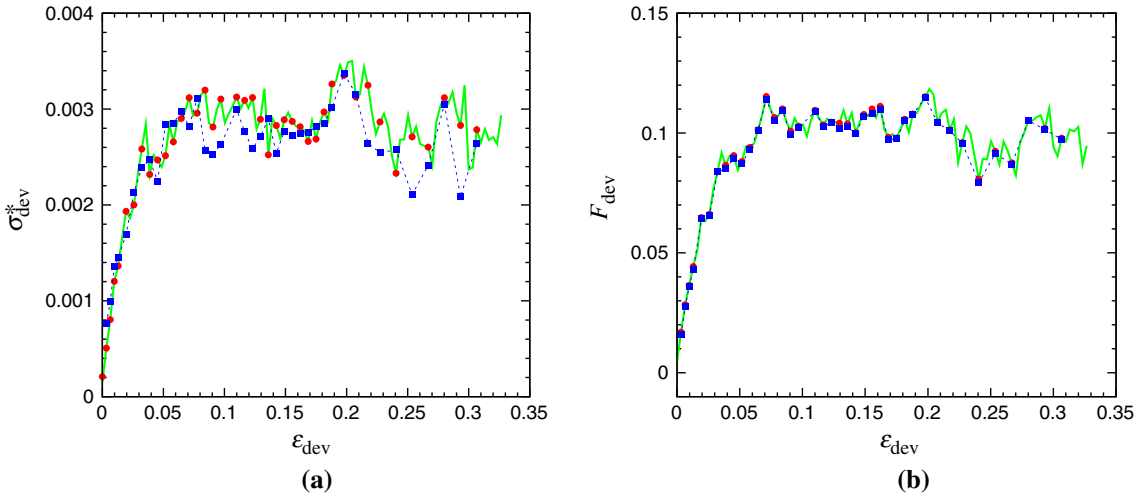

Fig. 5 Evolution of **a** non-dimensional shear stress σ^*_{dev} and **b** deviatoric fabric F_{dev}, along the main strain path ε_{dev} for the pure shear deformation mode, for volume fraction $\nu = 0.706$. The *red circle* symbols in **a**, **b** are the chosen states, which are first relaxed (*blue square* symbols in **a** and **b**) and then used as initial configurations for the purely isotropic $3\delta\varepsilon_v$ and purely deviatoric $\delta\varepsilon_{dev}$ perturbations (color figure online)

increase in stress and stiffness in the out-of-plane direction (z-direction here) due to the non-planar (triaxial) stress state associated with the plane deformation mode, is not independently accounted for. These are rather hidden in the expression for deviatoric stress as proposed in Eq. (9) and used in Eq. (11). However, we have chosen this representation, since advantages are obtained by investigating the elasticity of a granular material (e.g., soil), not by its resistance to direct stresses expressed by Young's modulus and Poisson's ratio, but rather in terms of (purely volumetric and deviatoric) stress response to volume and shape changes, as described by the bulk modulus B and the octahedral shell modulus G^{oct}. This aspect will be further addressed in Sect. 5, where Eq. (11) will be included in the theoretical model.

To study the evolution of the effective moduli during shear, we choose different initial states (forty) as shown in Fig. 5, and apply sufficient relaxation, so that the granular assemblies dissipate the kinetic energy accumulated during the original shearing path. When the states along the shear path are relaxed, a much higher change is visible in σ^*_{dev} rather than in F_{dev}, see Fig. 5. This shows that the contact network remains almost intact and F_{dev} does not change; on the other hand, the average particle overlap is more sensitive to the relaxation stage and decreases (in steady state), leading to a finite drop in σ^*_{dev}. Then we perform a small strain perturbation to these relaxed anisotropic states, i.e., we probe the samples, and measure the incremental stress response [40,50]. Finally, the elastic moduli are calculated as the ratio between the measured increment in stress and the applied strain. We obtain all the different moduli in Eq. (11), by applying an incremental pure volumetric or pure deviatoric strain and measuring the incremental volumetric or shear stress response:

$$B = \left.\frac{\delta P^*}{3\delta\varepsilon_v}\right|_{\delta\varepsilon_{dev}=0}, \; A_1 = \left.\frac{\delta P^*}{\delta\varepsilon_{dev}}\right|_{\delta\varepsilon_v=0},$$
$$A_2 = \left.\frac{\delta\sigma^*_{dev}}{3\delta\varepsilon_v}\right|_{\delta\varepsilon_{dev}=0}, \; G^{oct} = \left.\frac{\delta\sigma^*_{dev}}{\delta\varepsilon_{dev}}\right|_{\delta\varepsilon_v=0}. \tag{12}$$

The system is allowed to relax again after the incremental strain is applied, that is both the stress and the change in stress are measured after relaxation [50,52]. Since the numerical probe experiments are carried out with zero contact friction, we are measuring the resistance of the frictionless material [40], where only normal forces are involved. The first big question concerns the amplitude of the applied perturbation to get the elastic response [6,21,72].

4.2 How small is small?

In this section, we discuss the amplitude of the perturbations applied to measure the elastic stress response of the granular material. Also, we will discuss the results for larger amplitudes and the threshold between elastic and plastic regimes.

4.2.1 Effect of isotropic perturbations $3\delta\varepsilon_v$

Figure 6 (column 1 and 2) shows the changes in non-dimensional pressure δP^*, non-dimensional shear stress $\delta\sigma^*_{dev}$, isotropic fabric δF_v and deviatoric fabric δF_{dev} for different amplitudes of the isotropic perturbation $3\delta\varepsilon_v$, applied to two relaxed states that have been sheared until $\varepsilon_{dev} = 0.0065$ (nearly isotropic configuration: column 1) and $\varepsilon_{dev} = 0.31$ (steady state configuration: column 2), respectively. The data correspond to the shear test with $\nu = 0.706$. The linear elastic response is also plotted (red solid curve) in the whole strain range, as derived from the incremental behavior at very small strain, to give an idea of the deviation from elasticity when strain increases.

δP^* initially increases linearly and smoothly with $3\delta\varepsilon_v$, in agreement with the prediction of linear elasticity. Also the difference between the two initial states (near isotropic and steady state as shown in Fig. 6a, b, respectively) is minimal, meaning that the bulk modulus B (slope of δP^* with $3\delta\varepsilon_v$ in the elastic regime) is almost constant. This is not surprising, as we expect B to be dependent on isotropic quantities that stay mostly unchanged during the shear deformation, as discussed in Sect. 4.3. $\delta\sigma^*_{dev}$ behaves similar as δP^* for small strain, but shows several sharp drops for large strain. These correspond to sudden changes in the coordination number δC^* (see Fig. 7a, b), due to rearrangements in the system during the probe. For the nearly isotropic state (Fig. 6e), the ratio of $\delta\sigma^*_{dev}$ with $3\delta\varepsilon_v$ in the linear elasticity regime, i.e., A_2, is small when compared with the steady state (Fig. 6f). This clearly tells that A_2 evolves during the shear deformation for a given volume fraction, and must be linked with deviatoric quantities.

δF_v increases with $3\delta\varepsilon_v$, with more fluctuations compared with δP^*, for both states considered here, $\varepsilon_{dev} = 0.0065$ (nearly isotropic state Fig. 6i) and $\varepsilon_{dev} = 0.31$ (steady state, Fig. 6j). Moreover, the prediction using Eq. (8) for F_v matches the dataset very well. F_{dev} does not change ($\delta F_{dev} = 0$) with increasing $3\delta\varepsilon_v$, until the first rearrangement in the structure occurs (see Fig. 7c, d). After this δF_{dev} starts to decrease with increasing amplitude $3\delta\varepsilon_v$, faster in the steady state (Fig. 6m) than in the near isotropic state, see Fig. 6n. We note here that, when a non-incremental volumetric strain ($3\delta\varepsilon_v > 10^{-4}$) is applied, the system moves from a volume-conserving to a new non-volume-conserving deformation path. As this system is already anisotropic, this leads to a decrease ($\delta F_{dev} < 0$) in deviatoric fabric F_{dev}, opposite to the increase ($\delta\sigma_{dev} > 0$) in deviatoric stress, see Fig. 6e, f, higher in the steady state (Fig. 6n) than in the nearly isotropic state (Fig. 6m). The last observation suggests that the distance between the volume-conserving and non-volume-conserving configurations increases with ε_{dev}.

Hence, during isotropic compression (increasing $3\delta\varepsilon_v$) of a pre-sheared (anisotropic) state, both the pressure P^* and shear stress σ^*_{dev} increase, with pressure increasing much faster leading to a decrease in deviatoric stress ratio $s_{dev} = \sigma^*_{dev}/P^*$. The deviatoric fabric F_{dev} also decreases with isotropic compression of a pre-sheared state, and the decrease is initially faster than the exponential decay of F_{dev} (see Sect. 5 below) with volume fraction ν, as seen in Fig. 6n. This decrease in F_{dev} becomes slower for large strain, as also seen in Fig. 6m. These observations are consistent with the findings of Imole et al. [30], where the authors noticed a decreasing steady state deviatoric fabric and deviatoric stress ratio with increasing volume fraction, or ε_v.

4.2.2 Effect of deviatoric perturbations $\delta\varepsilon_{dev}$

Figure 6 (column 3 and 4) shows the changes in the same quantities as before for different amplitudes of the deviatoric perturbation $\delta\varepsilon_{dev}$, applied to a relaxed state with volume fraction $\nu = 0.706$ that has been sheared until $\varepsilon_{dev} = 0.0065$ (nearly isotropic configuration: column 3) and $\varepsilon_{dev} = 0.31$ (steady state configuration: column 4).

δP^* increases linearly with $\delta\varepsilon_{dev}$ (the slope in the elastic regime is A_1), with A_1 much smaller for the nearly isotropic state (Fig. 6c) than for the steady state (Fig. 6d). This shows that A_1 evolves during the shear deformations, like A_2, for a given volume fraction, and must be linked with the deviatoric state of the system. Moreover, after large deformation, both states show drops in δP^*, which can be linked to the particle rearrangements (see Fig. 7c, d). A nonlinear, irregular behavior shows up for $\delta\varepsilon_{dev} > 10^{-4}$, with δP^* positive in case of loose sample (present sample) and negative for dense samples (data not shown), in agreement with

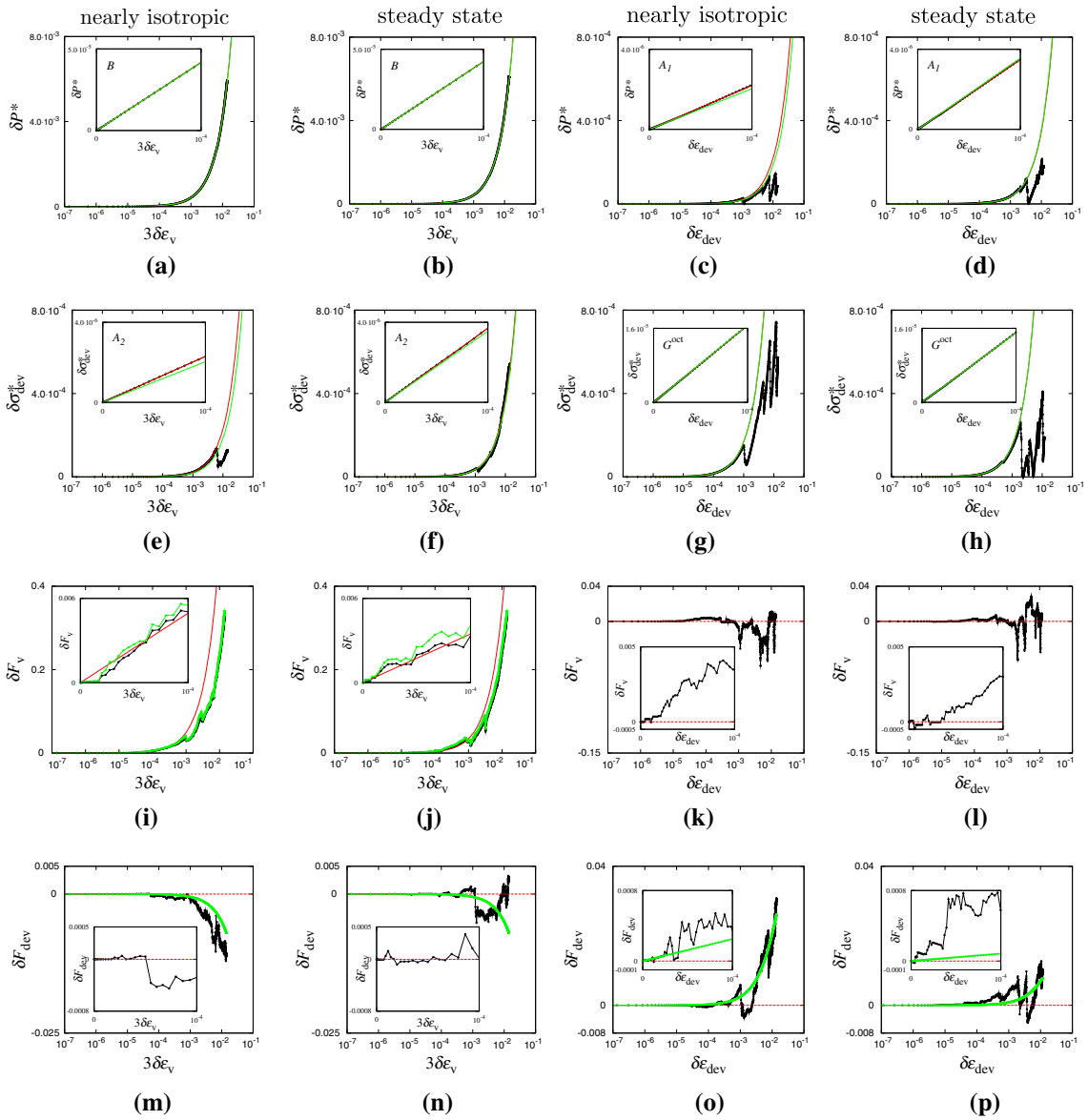

Fig. 6 (*Rows*) Evolution of the incremental non-dimensional pressure δP^*, non-dimensional shear stress $\delta\sigma^*_{\rm dev}$, isotropic fabric $\delta F_{\rm v}$ and deviatoric fabric $\delta F_{\rm dev}$ versus strain amplitude. *Columns* 1 and 2 represent purely isotropic while *columns* 3 and 4 represent deviatoric perturbation experiments. The perturbation is applied to the state corresponding to $\varepsilon_{\rm dev} = 0.0065$ (nearly isotropic configuration: *columns* 1 and 3) and $\varepsilon_{\rm dev} = 0.31$ (steady state configuration: *columns* 2 and 4) of the main deviatoric experiment with volume fraction $\nu = 0.706$. Note that the x axis is log-scale, with *inset* plots in linear scale. The *red line* passing through the dataset in **a**–**j** represents a linear fit in the elastic regime for $3\delta\varepsilon_{\rm v}$; $\delta\varepsilon_{\rm dev} < 10^{-4}$. The analytical predictions for the elastic range from our results Sect. 4.3 in Eqs. (13)–(17) are plotted as *green line* in **a**–**h**. The *green line* in **i** and **j** represents $F_{\rm v} = g_3\nu C$ calculated using Eq. (8), when subtracted from its initial value. The *dashed horizontal line* in **k**–**p** represents zero. The *green line* in **m** and **n** represents the evolution of change in deviatoric fabric $\delta F_{\rm dev}$ in critical state using parameters from Table 3 of Ref. [30], with the assumption that the new state after volumetric deformation is also in critical state. The *green line* in **o** and **p** represents Eq. (18) from Ref. [30] when subtracted from its initial value $F^0_{\rm dev} = 0.03$ for **o** and $F^0_{\rm dev} = 0.113$ for **p**, with the growth rate $\beta_F = 39$ and $F^{\rm max}_{\rm dev} = 0.12$ (color figure online)

the observations in Fig. 2a. $\delta\sigma^*_{\rm dev}$ also increases linearly with $\delta\varepsilon_{\rm dev}$, with $G^{\rm oct}$ (slope of the line) slightly higher for the near isotropic state (Fig. 6g) than for the steady state (Fig. 6h). Again, similar to δP^*, $\delta\sigma^*_{\rm dev}$ shows drops after large deformations, which can be linked to the particle rearrangements (see Fig. 7c, d). In the steady state, the incremental stresses (δP^* and $\delta\sigma^*_{\rm dev}$) increase linearly for very small strain, as the relaxed configuration, starting point for the probes, has lower stress than the main deviatoric path (see Fig. 5a) and the system tends

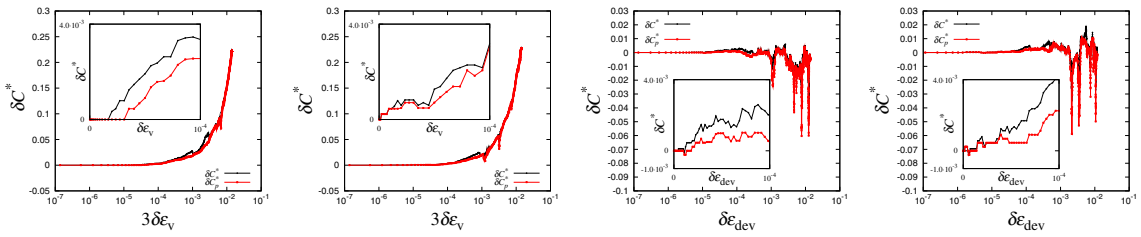

Fig. 7 Evolution of the incremental coordination number $\delta C^* = \delta\,(M_4/N_4)$ (*black circle* curve) and the modified coordination number $\delta C_p^* = \delta\left(M_4^p/N_4\right)$ (*red asterisk* curve), defined in Sect. 2, versus strain amplitude during purely **a**, **b** isotropic and **c**, **d** deviatoric perturbation experiments (corresponding plots as in Fig. 6). The perturbation is applied to the state corresponding to $\varepsilon_{\rm dev} = 0.0065$ [nearly isotropic configuration: **a** and **c**] and $\varepsilon_{\rm dev} = 0.31$ [steady state configuration: **b** and **d**] of the main deviatoric experiment with volume fraction $\nu = 0.706$. Note that the x axis is on log-scale, with *inset* plots in linear scale (color figure online)

to regain the "missed" stress, when the shear restarts. After the first elastic response, δP^* and $\delta\sigma^*_{\rm dev}$ fluctuate around zero for larger amplitudes (Fig. 6d, h), as no change in stress is expected with increasing deviatoric strain in the steady state.

$\delta F_{\rm v}$ stays mostly zero when small $\delta\varepsilon_{\rm dev}$ is applied for both near isotropic and steady state configurations (Fig. 6k, l). With increasing strain amplitude, $\delta F_{\rm v}$ increases in the case of a loose sample close to the isotropic state (Fig. 6k), and decreases for denser samples (data not shown), in agreement with the behavior in Fig. 2b. In Fig. 6o, $\delta F_{\rm dev}$ for the nearly isotropic state stays zero for $\delta\varepsilon_{\rm dev} < 10^{-4}$, when no rearrangements happen and the behavior is elastic, while it reaches a positive finite value for larger amplitude (that coincides with the slope of the curve in Fig. 3b). This finite value drops to zero in the steady state, where no variation of deviatoric fabric is expected with further applied deviatoric strain (see Fig. 6p). When compared with the model predictions in Ref. [30], the simulation data for $F_{\rm dev}$ well match with the theoretical line, where $F_{\rm dev}$ increases due to shear for the near isotropic state, and does not change for the steady state simulation.

4.2.3 Discussion and comparison

Since we are interested in measuring the pure elastic response of the material, we take care that no rearrangements happen in the system during the numerical probe, that is, $3\delta\varepsilon_{\rm v}$ and $\delta\varepsilon_{\rm dev}$ are applied only up to 10^{-4} (with very slow wall movement $\approx 10^{-5}[{\rm s}^{-1}]$, i.e., smaller than for the main large shear strain preparation experiment). Looking at Fig. 6, we note that much bigger drops appear in the deviatoric response when the isotropic perturbation is applied. Vice versa, the fluctuations/drops are much larger in pressure rather than in shear stress, when we deal with deviatoric perturbations. It is worthwhile to mention here that we have tested our method by applying strain perturbations in opposite directions i.e., $3\delta\varepsilon_{\rm v}$ and $-3\delta\varepsilon_{\rm v}$, $\delta\varepsilon_{\rm dev}$ and $-\delta\varepsilon_{\rm dev}$. This does not lead to any difference in the elastic response, as long as we stay in the limit of elastic perturbations.

We test the rearrangements argument in Fig. 8, by plotting the calculated bulk modulus B and octahedral shear modulus $G^{\rm oct}$ against the amplitude of the applied isotropic $3\delta\varepsilon_{\rm v}$ and deviatoric $\delta\varepsilon_{\rm dev}$ strain, respectively, for states at $\varepsilon_{\rm dev} = 0.0065$ and 0.31 (nearly isotropic and steady state configurations, respectively) of the main deviatoric experiment. Both B and $G^{\rm oct}$ stay practically constant for small amplitudes, and we can assume the regime to be linear elastic [10]. At $3\delta\varepsilon_{\rm v} \simeq 10^{-4}$, the first change in the number of contacts happens (Fig. 7a, b), and B starts to increase non-linearly. Similarly, when $\varepsilon_{\rm dev} \simeq 10^{-4}$, the first change in the number of contacts happens (Fig. 7c, d), and $G^{\rm oct}$ starts to decay. It is interesting to notice that for both B and $G^{\rm oct}$ the elastic regime shrinks when the main deviatoric strain $\varepsilon_{\rm dev}$ increases (Fig. 8) and, also, when the volume fraction reduces, going toward the jamming volume fraction (data not shown). A fabric modulus may be plotted as $\delta F_{\rm dev}/\delta\varepsilon_{\rm dev}$ that, due to the finite size of the system, would be identically zero, until the first change of structure (fabric) occurs (see Fig. 6).

We further check the elasticity of the probe by reversing the incremental strain. We plot the stress responses to volumetric/deviatoric strain in Fig. 9 and compare loading and unloading probes for different volume fractions ($\nu = 0.706$ and 0.812) and amplitudes. Looking at Figs. 6, 7 and 9 together, three regimes seem to appear. The first one at very small strain (on the order of 10^{-5}) is characterized by no opening and closing of contacts and shows perfect reversibility of the data, i.e., elasticity, in Fig. 9a–d. This is related with the finite size of the system. The second regime in Fig. 9(e–h) shows some weakly irreversible behavior, but only for the smaller

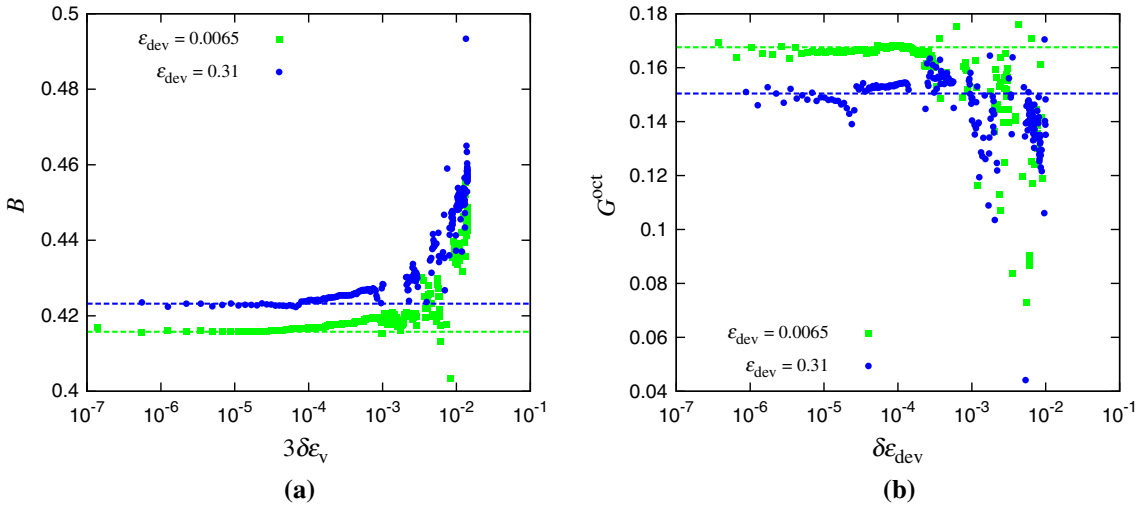

Fig. 8 Evolution of **a** bulk modulus B and **b** octahedral shear modulus G^{oct} with the respective applied isotropic $3\delta\varepsilon_{\text{v}}$ and deviatoric $\delta\varepsilon_{\text{dev}}$ strain amplitudes for a state corresponding to $\varepsilon_{\text{dev}} = 0.0065$ (nearly isotropic configuration: *green square*) and $\varepsilon_{\text{dev}} = 0.31$ (steady state configuration: *blue circle*) of the main deviatoric experiment with volume fraction $\nu = 0.706$. Corresponding *dashed horizontal lines* represents the initial values of B and G^{oct} (color figure online)

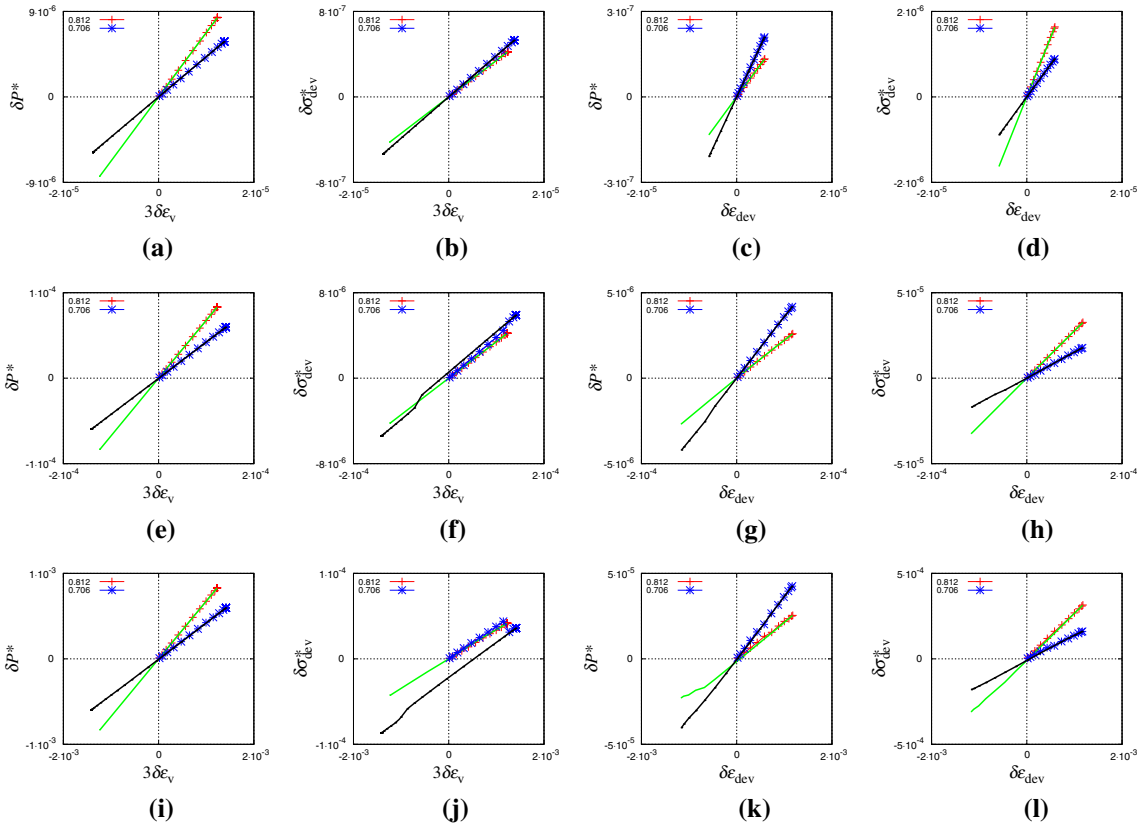

Fig. 9 Evolution of the incremental non-dimensional pressure P^*, non-dimensional shear stress σ^*_{dev} during small (**a**–**d**), medium (**e**–**h**), and large (**i**–**l**) perturbations in the loading (*symbols*) and then unloading (*solid lines*) direction. *Red plus symbols* represents loading and the *green line* represents unloading for $\nu = 0.812$. Similarly, *blue asterisk symbols* represents loading and the *black line* represents unloading for $\nu = 0.706$. The deformation is applied to the state corresponding to $\varepsilon_{\text{dev}} = 0.31$ (steady state configuration) of the main deviatoric experiment (color figure online)

volume fraction and a mixed perturbation mode, see the sample at $\nu = 0.706$ in Fig. 9f; we associate this behavior to minor contact changes, as visible in Figs. 6 and 7, but no large scale rearrangements occur. Finally, in the third regime, for perturbations two orders of magnitude higher (on the order of 10^{-3}), a residual strain after reversal shows up for both volume fractions and all types of perturbations, see Fig. 9i–l, proving also that plasticity is much more pronounced in the deviatoric modes than in isotropic ones. We claim that small drops are related to local (weak, almost reversible) re-structuring, while in the last case, the whole system (or a big portion of it) is involved in the collapse of the structure, with a more pronounced effect for samples close to the jamming volume fraction [35,49].

For granular materials, the strain cannot be split in elastic and plastic contributions by "trivially" referring to the residual deformation like in classical solids: as soon as we are out of the elastic range, rearrangements happen during loading and (even though less probably) during unloading, and most likely no original position is recovered for any particle. Finally, we note that the results shown here are valid for finite-size systems; for much larger (real) samples of much smaller particles, we expect the first elastic regime to reduce to much smaller strains. The transition between the second and third regime is an issue for further research [68].

4.3 Evolution of the moduli

Using five packings at different ν_i, we next determine which variables affect the incremental response of the aggregates at different deviatoric strains along the main path. In order to understand the role of the microstructure, i.e., the fabric tensor $\mathbf{F}$, the volumetric and deviatoric components, F_{v} and F_{dev}, are considered. We postulate that the incremental response of the granular material can be uniquely predicted, once its fabric state (along with the stress state) is known, irrespective of the path that the system experienced to reach that state. In this sense the fabric tensor can be referred to as a state variable.

4.3.1 Bulk modulus B

In Fig. 10a, we plot the incremental non-dimensional pressure δP^* against the amplitude of the applied isotropic perturbation $3\delta\varepsilon_{\mathrm{v}}$ for one volume fraction, $\nu = 0.706$, and various initial anisotropic configurations. The slope of each line is the bulk modulus of that state. It practically remains unchanged for different states and suggests that B is constant for a given volume fraction.

In Fig. 10b, we plot the variation of the bulk modulus B with the isotropic fabric F_{v} for packings with different volume fractions ν_i. B increases systematically when the five different reference configurations are compared, and it is related to the value of F_{v} constant at a given ν_i [24,40,70]. As expected B is a purely

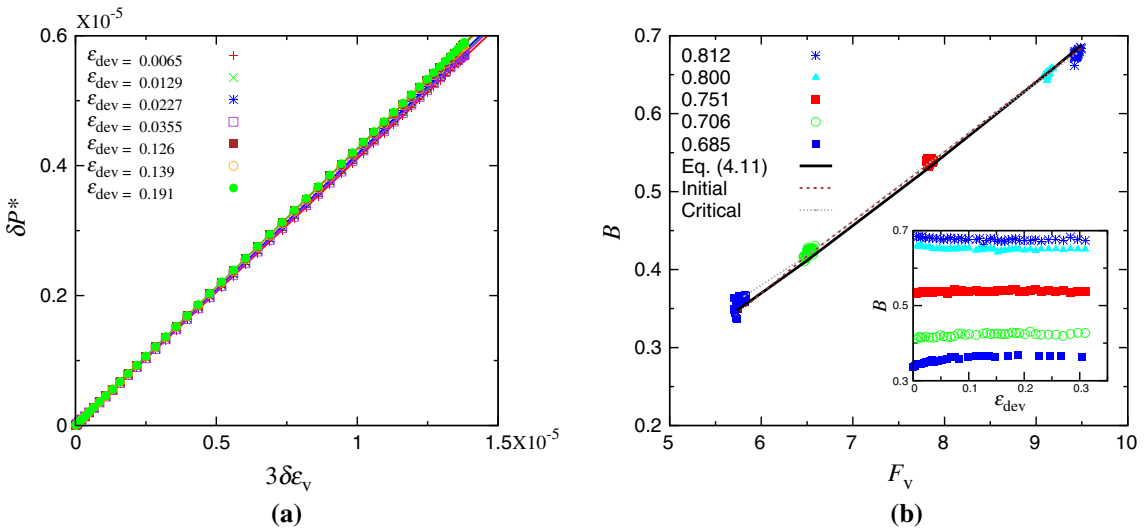

Fig. 10 **a** Evolution of the incremental change in non-dimensional pressure δP^* during purely isotropic perturbations $3\delta\varepsilon_{\mathrm{v}}$ for different states for volume fraction $\nu = 0.706$ along the main path as shown in the *inset*. **b** Evolution of the bulk modulus B as scaled with isotropic fabric F_{v} for five different volume fractions as shown in the *inset*. The *solid line* passing through the data represents Eq. (13). The *dashed lines* represent the initial and steady state data, as given in the legend (color figure online)

volumetric quantity and varies with changes in the isotropic contact network. The inset in Fig. 10b shows that the bulk modulus remains almost constant with applied shear during a single deviatoric experiment [40], behaving qualitatively similar to pressure P^* and isotropic fabric $F_{\rm v}$, see Figs. 1a and 3a, respectively. That is, the contact orientation anisotropy, $F_{\rm dev}$, which changes during the main deviatoric deformation path (see Fig. 3b) does not affect it. In agreement with observations on the volumetric fabric in Sect. 3.2, also B shows a slight increase/decrease in the first part of the deviatoric path, more pronounced for loose samples, as clearly seen in Fig. 2b. The trend of B slightly deviates from $F_{\rm v}$ in the low strain regime, while the dependence is well captured in the steady state, after large strain. The relation between bulk modulus and fabric was given in Ref. [24] as:

$$B = \left.\frac{\delta P^*}{3\delta\varepsilon_{\rm v}}\right|_{\delta\varepsilon_{\rm dev}=0} = \frac{p_0 F_{\rm v}}{g_3 \nu_c}\left[1 - 2\gamma_p\left(-\varepsilon_{\rm v}\right) + \left(-\varepsilon_{\rm v}\right)\left(1 - \gamma_p\left(-\varepsilon_{\rm v}\right)\right)\frac{\partial \ln F_{\rm v}}{\partial\left(-\varepsilon_{\rm v}\right)}\right], \tag{13}$$

where p_0, γ_p and the jamming volume fraction ν_c are fit parameters presented in Table 1.[4] $g_3 \approx 1.22$ is dependent on the particle size distribution as presented in Refs. [24,30,39], see Sect. 2. For a given volume fraction, the above relation only requires the knowledge of the isotropic fabric $F_{\rm v} = g_3 \nu C = g_3 \nu C^* (1 - \phi_r)$, where the empirical relations for $C^*(\nu)$ and $\phi_r(\nu)$ are taken from Refs. [30,39], see Sect. 2. The numerical data show good agreement with the theoretical prediction presented in [24] and reported in Fig. 10b. The minimum $F_{\rm v}$ is obtained at the jamming volume fraction, with $\nu_c = 0.658$, $C^* = 6$, and $\phi_r = \phi_c = 0.13$, leading to $F_{\rm v}^{\rm min} \approx 4.2$. At the jamming transition, we can extrapolate a finite value of the bulk modulus $B^{\rm min} = 0.22$, while it suddenly drops to zero below ν_c [14,31,55,62–65,85]. The discontinuity of B is related to the discontinuity in $F_{\rm v}$, that jumps from zero to a finite value at ν_c due to equilibrium requirements.

4.3.2 Anisotropy moduli A_1 and A_2

In Fig. 11a, we plot the non-dimensional pressure increment δP^* against the strain amplitude, when the material is subjected to small deviatoric perturbations $\delta\varepsilon_{\rm dev}$, to measure the first anisotropy modulus A_1 as defined in Eq. (12), in given anisotropic configurations, as in Fig. 10a. Since the material is in an anisotropic state, an increment in deviatoric strain leads to a change in volumetric stress, along with shear stress. The slope of the curves, A_1, increases with the previous shear strain the system has experienced, from small values in the initial isotropic configuration, to an asymptotic limit.

We are interested in the ratio A_1/B. In this ratio, the dependence of isotropic fabric $F_{\rm v}$ cancels out, all that remains is a pure dependence on $F_{\rm dev}$. In Fig. 11b, we plot the variation of A_1/B, with $F_{\rm dev}$ for packings with different volume fractions ν_i as shown in the inset. Besides the fluctuations, the data collapse on a unique curve irrespective of volume fraction and pressure, that is, once a state has been achieved, a measurement of the overall anisotropy modulus is associated with a unique $F_{\rm dev}$. An increasing trend of A_1/B with the deviatoric fabric shows up. As the deviatoric fabric decreases with volume fraction (see Fig. 3b), this leads to lower values of the scaled anisotropy modulus for denser systems. In conclusion, we have a linear relation between the first anisotropy modulus A_1 and fabric:

$$A_1 = \left.\frac{\delta P^*}{\delta\varepsilon_{\rm dev}}\right|_{\delta\varepsilon_{\rm v}=0} = a_{\rm I} B F_{\rm dev}, \tag{14}$$

where B is the bulk modulus, $F_{\rm dev}$ is the deviatoric part of fabric, and $a_{\rm I} \approx 1.0$ is a fit parameter presented in Table 1.

In Fig. 12a, we plot the stress response of the material $\delta\sigma^*_{\rm dev}$ to isotropic perturbation $3\delta\varepsilon_{\rm v}$, for the same anisotropic initial configurations as in Fig. 10a, to measure the second anisotropy modulus A_2 as defined in Eq. (12). Similarly to A_1, the slope of the elastic curves, i.e., A_2, increases with the previous shear strain the system has felt, starting form zero until an asymptotic limit is reached. In Fig. 12b, we plot the variation of A_2/B, with $F_{\rm dev}$ for different volume fractions ν_i as shown in the inset. Data show a very similar trend as in Fig. 11b, and besides the fluctuations, a collapse of data is observed.[5] Again we can relate A_2 to deviatoric fabric as

[4] Note that ν_c for the same particulate system was reported as 0.66 for isotropic deformation in Ref. [24], as 0.6646 for isotropic and 0.658 for shear deformation in Ref. [30]. We use a similar $\nu_c = 0.658$ here, which, however, is dependent on history of the sample and on the deformation mode. The small deviations of B from Eq. (13) can be attributed to a (small) variation of ν_c; however, this is beyond the focus of this paper.

[5] A large data scatter is present in both figures (Figs. 11b, 12b), which increases for increasing deviatoric fabric $F_{\rm dev}$. This is possibly due to other factors that may contribute to the evolution of the anisotropy moduli that are not considered in the present work.

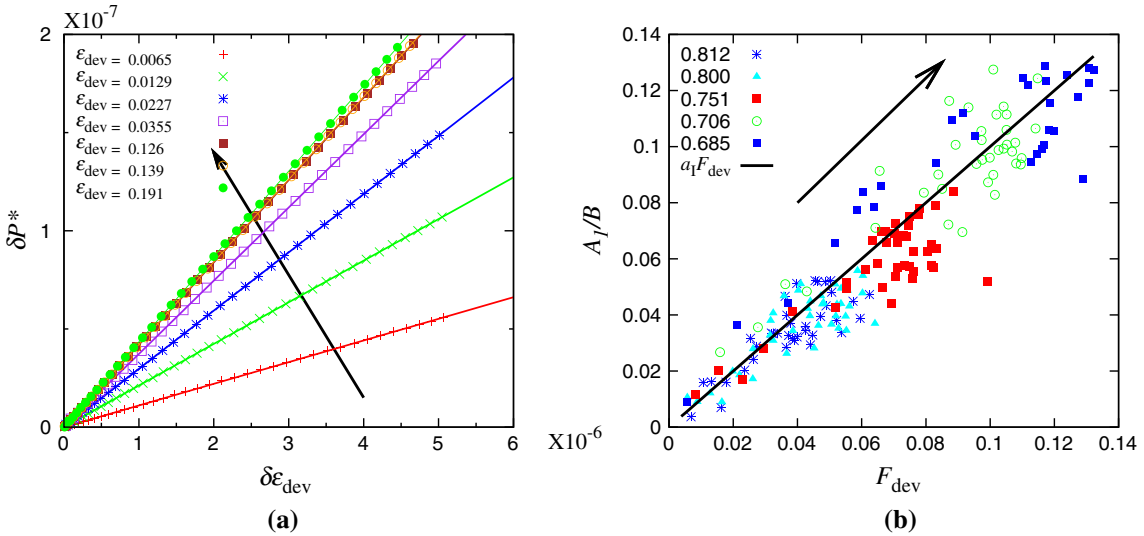

Fig. 11 **a** Evolution of the incremental change in non-dimensional pressure δP^* during purely deviatoric perturbations $\delta\varepsilon_{\text{dev}}$ for different states for volume fraction $\nu = 0.706$ along the main path as shown in the *inset*. The *arrow* indicates the direction of increasing strain states during main deviatoric experiments. **b** Evolution of the ratio of first anisotropy modulus with bulk modulus A_1/B as function of the deviatoric fabric F_{dev} for five different volume fractions as shown in the *inset*. The *solid line* passing through the data represents Eq. (14) divided by B (color figure online)

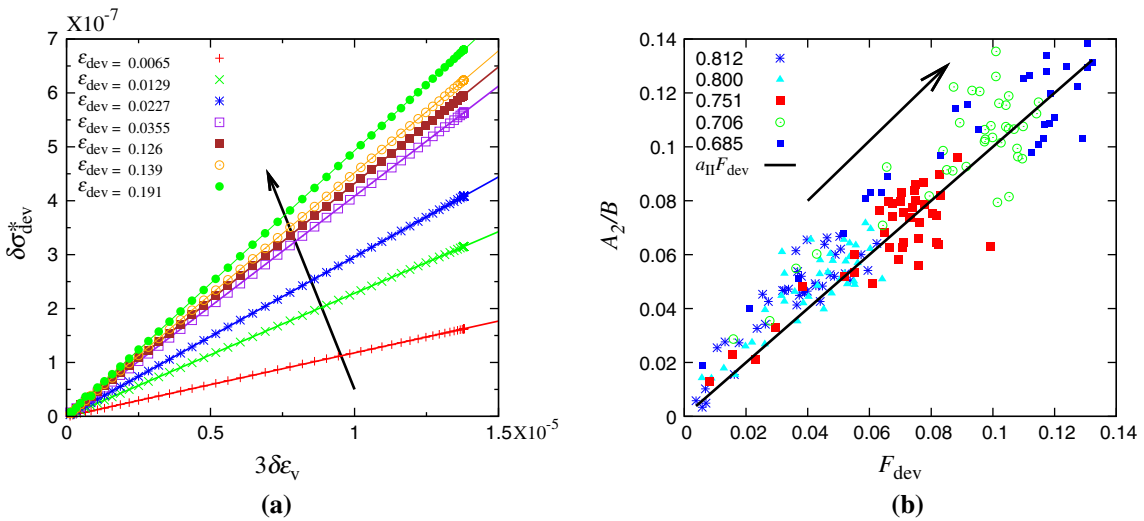

Fig. 12 **a** Evolution of the incremental change in non-dimensional shear stress $\delta\sigma^*_{\text{dev}}$ during purely isotropic perturbations $3\delta\varepsilon_{\text{v}}$ for different states for volume fraction $\nu = 0.706$ along the main path as shown in the *inset*. The *arrow* indicates the direction of increasing strains during main deviatoric experiments. **b** Evolution of the ratio of second anisotropy modulus with bulk modulus A_2/B as scaled with the deviatoric fabric F_{dev} for five different volume fractions as shown in the *inset*. The *solid line* passing through the data represents Eq. (15) divided by B (color figure online)

$$A_2 = \left.\frac{\delta\sigma^*_{\text{dev}}}{3\delta\varepsilon_{\text{v}}}\right|_{\delta\varepsilon_{\text{dev}}=0} = a_{\text{II}} B F_{\text{dev}}. \tag{15}$$

The equality between the two fitting constants $a_{\text{I}} \approx a_{\text{II}} \approx 1$ (see Table 1), establishes the symmetry of the stiffness matrix in Eq. (11).

Equations (14) and (15) provide an interesting, novel way to back-calculate the deviatoric structure in a granular sample via $F_{\text{dev}} = A/B$, where A and B can be inferred from wave propagation experiments, while the direct measurement of fabric is still an open issue [29,34,36,74].

Table 1 Summary of fit parameters extracted from the small perturbation results in Eqs. (13), (14), (15) and (17)

Modulus	Parameters
Bulk modulus B	$p_0 = 0.0425$, $\gamma_p \approx 0.2$, $\nu_c = 0.658$
First anisotropy modulus A_1	$a_{\mathrm{I}} = 1 \pm 0.01$
Second anisotropy modulus A_2	$a_{\mathrm{II}} = 1 \pm 0.02$
Octahedral shear modulus G^{oct}	$g_{\mathrm{I}} = 130 \pm 3$, $F_{\mathrm{v}}^{\alpha} \approx 1.9$

4.3.3 Octahedral shear modulus G^{oct}

In Fig. 13a, we plot the shear stress response $\delta\sigma^*_{\mathrm{dev}}$ of the material when the initial configurations in Fig. 10a are subjected to small deviatoric perturbations $\delta\varepsilon_{\mathrm{dev}}$. The octahedral shear modulus G^{oct} is then measured, as defined in Eq. (12). The slope of the curves for different initial configurations slightly decreases with the deviatoric state of the system, and saturates for high deformation $\varepsilon_{\mathrm{dev}}$, when the steady state is reached. Figure 13b shows the variation of G^{oct} against shear strain $\varepsilon_{\mathrm{dev}}$. G^{oct} starts from a finite value in the initial configuration, related to the isotropic contact network, and slightly decreases with increasing strain, with different rates for different volume fractions. The behavior of G^{oct} differs from that observed for the bulk modulus in the inset of Fig. 10b: the shear resistance consistently decreases with shear strain, and no transition between initial decrease/increase is observed, meaning that a factor other than F_{v} influences the change of G^{oct} during the deviatoric path. Similarly to what done for A_1 and A_2, we look at the ratio of the shear modulus with the bulk modulus G^{oct}/B plotted against the isotropic fabric F_{v} in Fig. 13c. The ratio increases with increasing F_{v}, with higher values in the initial state than in the steady state (data are averaged over shear strain $\varepsilon_{\mathrm{dev}} \leq 0.0065$ to get the initial value and in the steady state to get the final one). The isotropic ratio $\left(G^{\mathrm{oct}}/B\right)_{\mathrm{ini}}$ increases with F_{v}, following the empirical relation:

$$\left(G^{\mathrm{oct}}/B\right)_{\mathrm{ini}} = \left(G^{\mathrm{oct}}/B\right)_{\mathrm{max}} \left[1 - \exp\left(\frac{F_{\mathrm{v}} - F_{\mathrm{v}}^{\mathrm{min}}}{F_{\mathrm{v}}^{\alpha}}\right)\right] \tag{16}$$

where $\left(G^{\mathrm{oct}}/B\right)_{\mathrm{max}} \sim 0.51$ represents the maximum value of the ratio G^{oct}/B for large F_{v} (or volume fraction), $F_{\mathrm{v}}^{\mathrm{min}} \sim 4.2$ (see Sect. 4.3.1) and $F_{\mathrm{v}}^{\alpha} \sim 1.9$ are the volumetric fabric and the rate of growth of $(G^{\mathrm{oct}}/B)_{\mathrm{ini}}$ at jamming transition. This is in agreement with previous studies that find an upper limit equal 0.5 for the ratio between the shear and bulk moduli [18,38,50,73]. In the limit of high F_{v}, the granular assembly becomes highly coordinated and practically follows the affine approximation that predicts a constant value for the ratio G^{oct}/B [78]. Here, a qualitatively similar behavior is observed for the values in the steady state, approaching a saturation ratio lower than the isotropic one.

Next, in Fig. 13d, we subtract the initial value $\left(G^{\mathrm{oct}}/B\right)_{\mathrm{ini}}$ from G^{oct}/B and assume that F_{v} does not change during the deviatoric deformation. Interestingly, we find that in this case the deviatoric microstructure alone is not able to capture the variation of the modulus along the shear path, but both stress $\boldsymbol{\sigma}$ and fabric $\mathbf{F}$ seem to influence the incremental shear response, in agreement with findings in [87]. We relate the decrease in G^{oct} to the deviatoric components of stress and fabric via:

$$G^{\mathrm{oct}} = \left.\frac{\delta\sigma^*_{\mathrm{dev}}}{\delta\varepsilon_{\mathrm{dev}}}\right|_{\delta\varepsilon_{\mathrm{v}}=0} = B\left[\left(\frac{G^{\mathrm{oct}}}{B}\right)_{\mathrm{ini}} - g_{\mathrm{I}}\sigma^*_{\mathrm{dev}}F_{\mathrm{dev}}\right] \tag{17}$$

where σ^*_{dev} is the non-dimensional shear stress, F_{dev} is the deviatoric fabric, and $g_{\mathrm{I}} \approx 130$ is a fit parameter reported in Table 1. Two contributions of the fabric to the shear stiffness can be recognized—isotropic and deviatoric. The overall contribution is multiplicative proportional to B, related to the isotropic contact network and changing very little with deviatoric strain. In the bracket, the first term gives the resistance of the material in the initial isotropic configuration, whereas the second part only depends on the deviatoric (state) variables and characterizes the evolution of the shear modulus with deviatoric strain. Given the initial isotropic configuration, the corresponding G^{oct} is known [16,50,78]; on the other hand, the anisotropic network of such a configuration uniquely defines the reduction in the shear stiffness. The product of deviatoric stress and fabric $\sigma^*_{\mathrm{dev}}F_{\mathrm{dev}}$ as proposed in [77,87] is able to capture the evolution of the ratio of the elastic moduli along the whole undrained

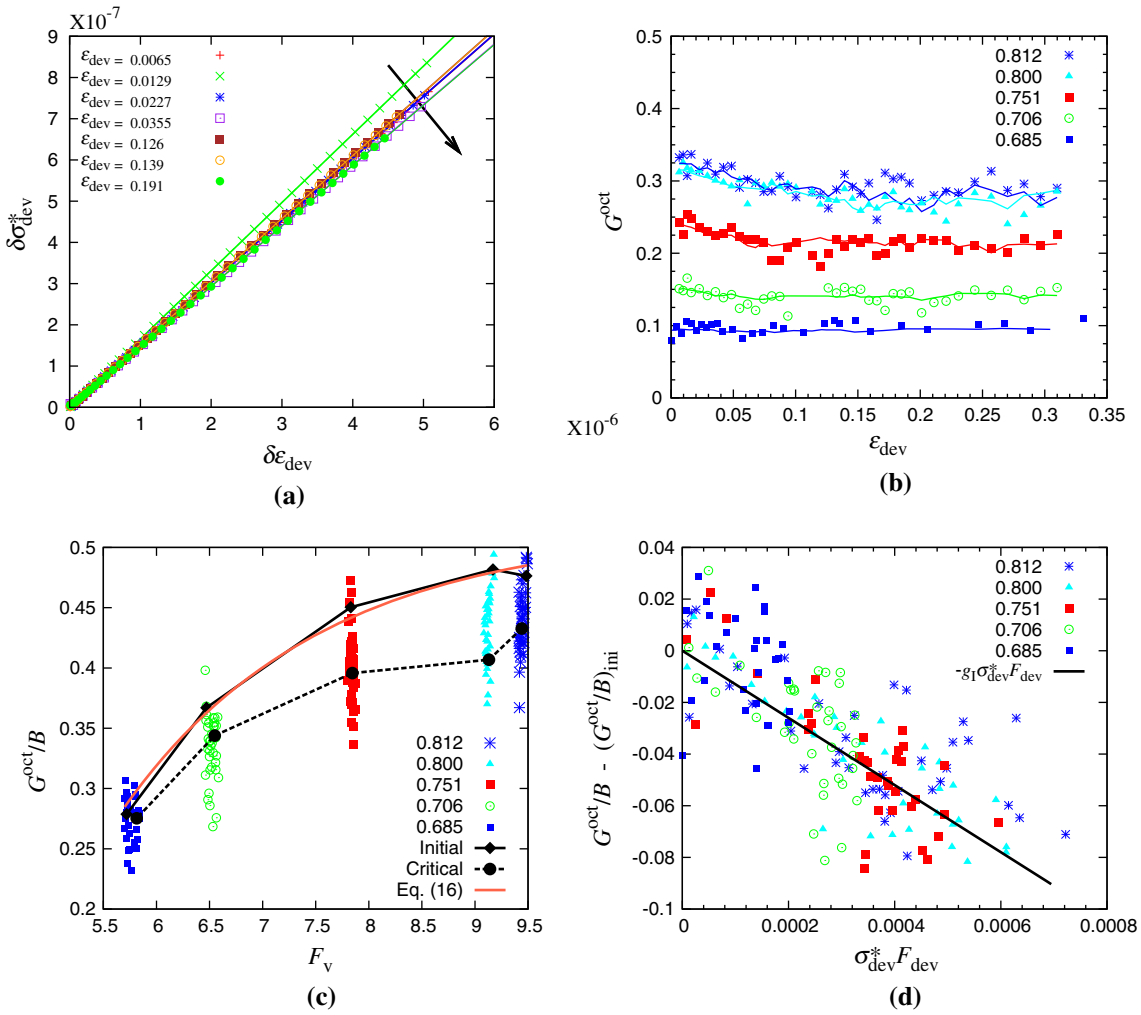

Fig. 13 **a** Evolution of the incremental change in shear stress $\delta\sigma^*_{\rm dev}$ versus strain amplitude during purely deviatoric perturbations $\delta\varepsilon_{\rm dev}$ for different states, with volume fraction $\nu = 0.706$, along the main path as shown in the *inset*. **b** Evolution of octahedral shear modulus $G^{\rm oct}$ along the main deviatoric path $\varepsilon_{\rm dev}$ for five different volume fractions as shown in the *inset*. The corresponding *lines* passing through the data represent Eq. (17). **c** Evolution of ratio of octahedral shear modulus and bulk modulus, i.e., $G^{\rm oct}/B$ with isotropic fabric $F_{\rm v}$, together with the averaged values at the initial (near isotropic state averaged over shear strain $\varepsilon_{\rm dev} \leq 0.0065$) and the steady state (averaged dataset in the steady state), as given in the legend. Note that the difference between initial and steady state increases with denser systems. The *solid orange line* passing through the isotropic dataset represents Eq. (16). **d** Evolution of the ratio of octahedral shear modulus and bulk modulus when its initial value, i.e., $G^{\rm oct}/B - \left(G^{\rm oct}/B\right)_{\rm ini}$ is subtracted, plotted using Eq. (17), for five different volume fractions as shown in the *inset* (color figure online)

path, as seen in Fig. 13d.[6] No other relation with volumetric quantities needs to be considered, as the evolution of $\sigma^*_{\rm dev} F_{\rm dev}$ depends on the volume fraction of the sample ν_i.

Note that when $G^{\rm oct}/B$ is plotted against $F_{\rm v}$ in Fig. 13c, a deviation from the fitting law is observed for each volume fraction, showing that extra correction terms might be needed for a more accurate description. This is neglected in this preliminary work. It is interesting to point out that the isotropic fabric has different effects in case of the anisotropy moduli A_1, A_2 and $G^{\rm oct}$, as in the former two cases $F_{\rm v}$, through B, is multiplied to $F_{\rm dev}$ and contributes to the growth of the moduli from zero to the asymptotic values, while in the latter case $F_{\rm v}$ defines mostly the initial values of $G^{\rm oct}$ via the bulk modulus, but does not affect the further decrease.

[6] Such a split between isotropic and deviatoric fabric influence applies to this specific deformation path, where the volume is conserved. Additional terms may enter when non-volume-conserving deformation paths are considered. A very similar behavior is observed when the definition in Eq. (6) is employed for the deviatoric fabric.

5 Prediction of undrained cyclic shear test

In this section, the constitutive model is presented, involving the elastic moduli measured and calibrated in Sect. 4, and the plastic response of the material under large strain. The model is then used to predict the material response under cyclic shear, involving reversal.

5.1 Calibration: constitutive model with anisotropy

We introduce here a constitutive model as proposed in Refs. [30,37,39,48,51], extended to three dimensions, that takes into account the evolution of fabric, independently of stress:

$$\begin{aligned} \delta P^* &= B3\delta\varepsilon_{\mathrm{v}} + AS_\sigma \delta\varepsilon_{\mathrm{dev}}, \\ \delta\sigma^*_{\mathrm{dev}} &= A3\delta\varepsilon_{\mathrm{v}} + G^{\mathrm{oct}} S_\sigma \delta\varepsilon_{\mathrm{dev}}, \\ \delta F_{\mathrm{dev}} &= \beta_F \mathrm{sign}\,(\delta\varepsilon_{\mathrm{dev}})\, F^{\mathrm{max}}_{\mathrm{dev}} S_F \delta\varepsilon_{\mathrm{dev}}. \end{aligned} \tag{18}$$

In its simple, reduced form, the model involves only three moduli B, A and G^{oct}, defined in the previous section in Eqs. (13)–(17). Due to A, the model provides a cross-coupling between the two types of stress and strain in the model, namely the isotropic stress P^* and shear stress σ^*_{dev} reacting to both isotropic (ε_{v}) and deviatoric ($\varepsilon_{\mathrm{dev}}$) strains. F_{dev} evolves differently from stress, as the rate of change with deviatoric strain can be (and in many cases is) different from the respective rate for the shear stress evolution. Note that additional terms (cross-coupling of fabric with strain) might be needed for the incremental evolution of δF_{dev} in Eq. (18), due to the observations from Fig. 6m, k, where F_{dev} and F_{v} change also with ε_{v} and $\varepsilon_{\mathrm{dev}}$, respectively. However, both cross-terms appear to be mostly activated in the highly anisotropic state, with values of the out-of-plane fabric considerably smaller than out-of-plane stress—but this has to be confirmed by other deformation paths also, i.e., we claim that some features are related to the specific deformation path proposed here. If a dependence between stiffness and fabric similar to that proposed in Eqs. (14) and (15) is assumed, previous arguments also lead to the conclusion that the out-of-plane stiffness terms developing during plane strain and neglected in Eq. (11) must be small compared with B, A and G. For the sake of simplicity, both evolution of cross-coupling fabric terms and out-of-plane stiffness are neglected in the present work, and postponed to future investigations, for the description of arbitrary deformation paths. The use of non-frictional particles is another possible reason for the simplest model to work astonishingly well—so the general model is expected to show all contributions for arbitrary deformation, in the presence of friction.

$S_\sigma = S/S^I_\sigma$, with $S = (1 - s_{\mathrm{dev}}/s^{\mathrm{max}}_{\mathrm{dev}})$ is a measure of the stress isotropy with normalized shear stress ratio $s_{\mathrm{dev}} = \sigma^*_{\mathrm{dev}}/P^*$, and S^I_σ is the initial stress isotropy at the start of a new deformation direction and/or after relaxation. $1 - S_\sigma$ is the measure for the probability of plastic events. Similarly, $S_F = (1 - F_{\mathrm{dev}}/F^{\mathrm{max}}_{\mathrm{dev}})/S^I_F$ is the fabric isotropy, and S^I_F is the initial fabric isotropy at the start of a new deformation direction and/or after relaxation. $s^{\mathrm{max}}_{\mathrm{dev}}$ and $F^{\mathrm{max}}_{\mathrm{dev}}$ represent the maximum (saturation) values of normalized shear stress ratio s_{dev} and deviatoric fabric F_{dev}, respectively, and β_F is the rate of change in F_{dev} at smaller strains (as shown in Fig. 3b).

It is worthwhile to point out that the definitions of S_σ and S_F are different from those used in Refs. [48,51], as both S_σ and S_F are now scaled by the initial reference value and can take values between 0 and 1. Due to S_σ and S_F, the incremental response of the material is purely elastic, after relaxation or at strain reversal, with the elastic moduli evolving, as given by Eqs. (13)–(17), as functions of the momentary stress and structure states. At reversal, the probability for plastic deformation drops to zero, and plastic events—as related to the approach to steady state—only occur after relatively large strain, that is, the reversal stiffness is not affected. Due to S_σ and S_F, the incremental response of the material in the large strain steady state ($S = 0$) becomes elastic ($S = 1$), just when the strain is reverted, or after relaxation (which is allowed before the probes). Due to the dependence of the elastic moduli on the stress/fabric state, the model involves nonlinear elasticity in its present form (without contact nonlinearities), while plasticity due to rearrangements is entirely associated with S_σ. On the other hand, the equation that describes the evolution of fabric is "purely plastic," as there is no change in fabric ($\delta F_{\mathrm{v}} = 0$), in the elastic regime, when no contact opening/closing and no multi-particle rearrangement happen.[7] Thus, the rate β_F is associated with changes of structure with deviatoric (shear) strain amplitude (not rate); changes are becoming more and more probable when approaching the steady state.

[7] We want to point out here the difference between the nonlinear elasticity built up along the main deviatoric path and the incremental elasticity, related to the small perturbations. Let's select two states A-B along the deviatoric path as indicated by

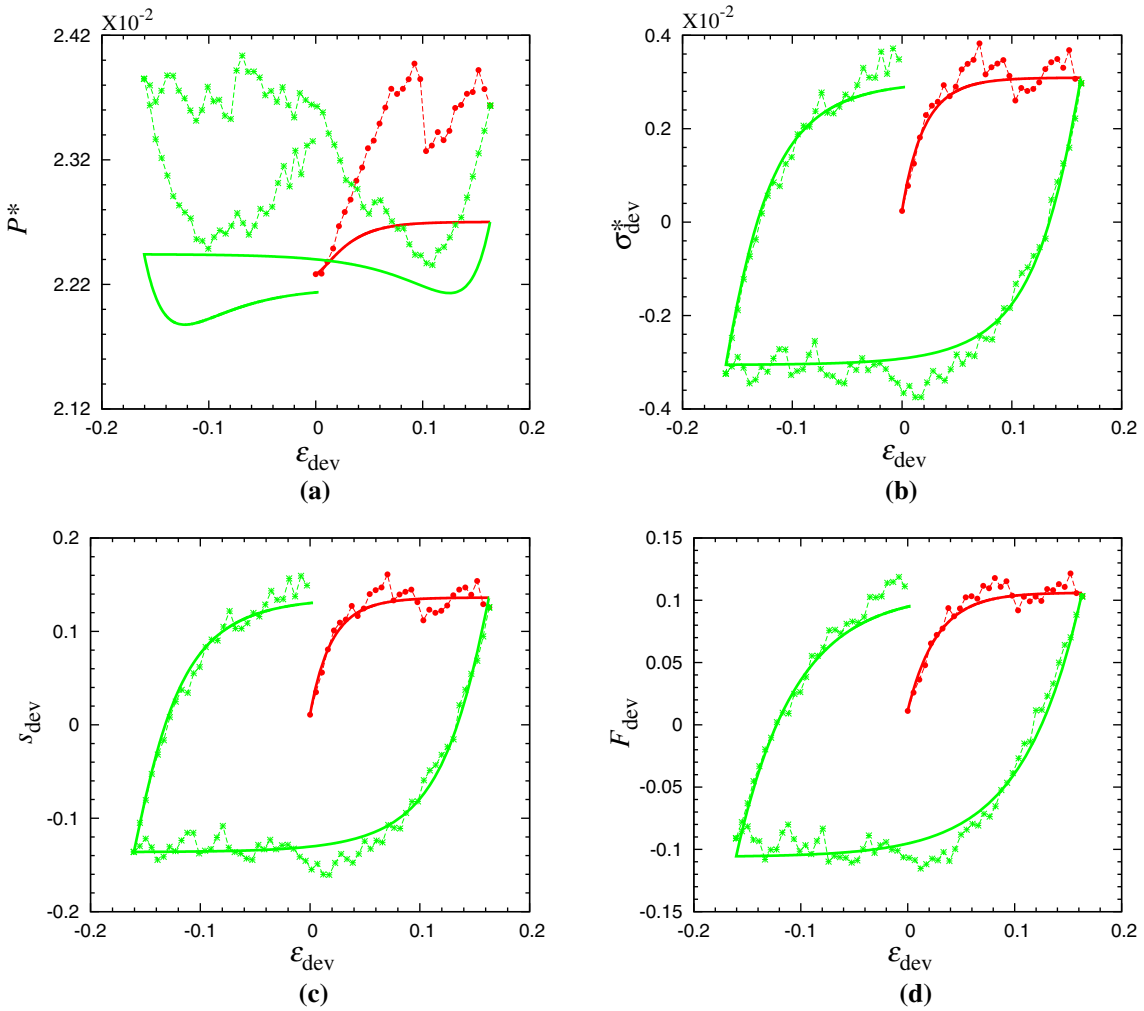

Fig. 14 Evolution of **a** pressure P^*, **b** deviatoric (shear) stress $\sigma^*_{\rm dev}$, **c** normalized shear stress $s_{\rm dev}$, and **d** deviatoric fabric $F_{\rm dev}$ with shear strain $\varepsilon_{\rm dev}$ during cyclic shear at constant volume $\nu = 0.711$, starting from an initial isotropic configuration. The values of $s^{\rm max}_{\rm dev}$, $F^{\rm max}_{\rm dev}$ and β_F for $\nu = 0.711$ are 0.167, 0.124 and 40.04, respectively, taken directly from the relations proposed in Refs. [30,39]. The *red circle* data points are the DEM simulation data over which the calibration of moduli was done, while the *green asterisk* data points represent unloading (reversal) and re-loading. The *solid line* is the prediction of the DEM observations using Eq. (18) (color figure online)

Now, we can predict an independent experiment, by using Eq. (18), and the relations between the three moduli B, A and $G^{\rm oct}$ with microscopic state variables given by Eqs. (13)–(17) with the numerical scaling factors from Table 1 (starting from B, we express the other moduli using their ratio with B). Moreover, three other parameters $s^{\rm max}_{\rm dev}$, $F^{\rm max}_{\rm dev}$ and β_F are needed to fully solve the coupled Eq. (18). The dependence of $s^{\rm max}_{\rm dev}$, $F^{\rm max}_{\rm dev}$ and β_F on volume fraction ν is well described by the exponential decay relation proposed in Refs. [30,39], where constant values, as given in Fig. 14 are used, as the volume is conserved during the cyclic shear test, as discussed next.

5.2 Prediction: (undrained) cyclic shear test

We choose an initial isotropic configuration, with volume fraction $\nu = 0.711$ and apply deviatoric (volume conserving) shear for one cycle: loading, unloading and final re-loading, to recover the initial box configuration.

Footnote 7 continued
points in Fig. 5, the incremental measured elastic response (moduli) is different between states A and B as it depends on stress and fabric, that is, the stiffness matrix in Eq. (11), varies non-linearly with $\varepsilon_{\rm dev}$. On the other hand, when the incremental strain $\delta\varepsilon_{\rm dev}$ is applied to each state (e.g., A or B), the incremental response is linearly elastic (by definition of incremental) and becomes plastic for high $\delta\varepsilon_{\rm dev}$, when rearrangements happen and the moduli in that given state go from elastic to plastic.

Figure 14 shows the evolution of pressure P^*, shear stress $\sigma^*_{\rm dev}$, shear stress ratio $s_{\rm dev}$ and deviatoric fabric $F_{\rm dev}$ with deviatoric shear strain $\varepsilon_{\rm dev}$ for one cycle, compared with the prediction using Eq. (18). Since the initial configuration is isotropic, the shear stress $\sigma^*_{\rm dev}$ and $F_{\rm dev}$ start from zero and approach saturation values (with fluctuations) at large strains. During reversal, both drop from their respective saturation value and decrease with unloading strain, crossing their zero values at different strain levels, and finally reach their steady state with negative signs. This supports the need of independent descriptions for the evolution of stress and fabric. Finally, re-loading is applied to reach the initial box configuration.

The qualitative behavior of pressure P^* is similar in simulations and model, going from a finite initial value to saturation with much less pronounced variations, since the deformation path is volume conserving. It is also interesting that the final state after the complete cycle, which corresponds to the initial box configuration, is highly anisotropic (non-zero stress $\sigma^*_{\rm dev}$ and deviatoric fabric $F_{\rm dev}$).

Both, the shear stress $\sigma^*_{\rm dev}$ and deviatoric fabric $F_{\rm dev}$, as well as their responses during strain reversal are well predicted by the model. P^* increases during loading $\varepsilon_{\rm dev}$ by $\sim 9\%$ and saturates at large strains. After reversal, P^* drops because of opening and release of contacts and then increases again with unloading strain. Although P^* is not quantitatively predicted by Eq. (18), the qualitative behavior is captured by the model, which requires a correction as proposed by Krijgsman and Luding [37]. The concept of a history-dependent jamming point, introduced by Kumar and Luding [41], is capable of capturing the behavior of P^* quantitatively; however, this goes beyond the scope of this study.

Equations (18) are able to describe the volumetric/deviatoric behavior of a granular assembly, in terms of stress and fabric. Once the initial state and the deformation path are defined, the evolution of isotropic fabric can be determined (using the coordination number and the fraction of rattlers) along the deformation path. The knowledge of isotropic and deviatoric fabric and the incremental relations in Eq. (18) allow for the definitions of the moduli at each incremental step. Given also the probabilities for the plastic events ($1 - S_\sigma$ and $1 - S_F$), the coupled system can be solved. That is, the characterization of the initial state is the information needed to fully describe the behavior of the material along a general deformation path, defined in terms of strain, since the incremental evolution equations for both stress and structure are given.

In the case of granular matter, the concept of a (homogeneous) material point in a continuum model is debated, and many studies have been devoted to the introduction of a length scale in the constitutive model, starting from the Cosserat brothers, see [11,44,53] among others. Here we limit ourselves and state that a finite-size system is always needed, in order to calibrate a continuum model. Every model interpretation works only between the upper/lower bounds of infinite system and particle scale. When a finite-size system is considered an elastic range can always be detected, such that rearrangements happen (see Sect. 4.2) with negligible(tiny) probability for very small strain, and an elasto-plastic framework could then make sense. In this work we introduce a local rate-type model in Eq. (18), and identify elasticity as the unique initial, static, configuration, from which the (incrementally irreversible) evolution of stress and structure follows. Our choice is to reduce elasticity to a "punctual range," as plastic deformations (which include irreversible opening/closing of contacts by large scale rearrangements) will dominate for large deformations. Dynamics and kinetic fluctuations, leading to relaxation, are not considered here, but also need to be taken into account, see e.g., [33].

6 Summary and outlook

In a triaxial box, the four elastic moduli that describe the incremental, elastic constitutive behavior of an anisotropic granular material in terms of volumetric/deviatoric components, namely the bulk modulus B, the two anisotropic moduli A_1, A_2 and the octahedral shear modulus $G^{\rm oct}$, can be measured by applying small strain perturbations to relaxed states that previously experienced a large strain along a volume-conserving (undrained) shear path. A connection between the macroscopic elastic response and the micromechanics is established, by considering both stress and fabric tensors, $\boldsymbol{\sigma}$ and $\mathbf{F}$, respectively. While the bulk modulus B depends on the isotropic contact network $F_{\rm v}$, the deviatoric component of the fabric tensor $F_{\rm dev}$ is the fundamental state variable determining the ratios between the (cross-coupling) anisotropic and bulk moduli. When the deviatoric stress and strain are appropriately scaled (normalized), we find that the moduli reduce to three relevant ones, i.e., $A = A_1 = A_2 = a F_{\rm dev} B$, with $a \approx 1$. The anisotropy moduli are related to both deviatoric and isotropic fabric, as the whole contact network determines how the system will react to a perturbation. Surprisingly, when the shear resistance $G^{\rm oct}$ is considered, both the contact network and the deviatoric stress determine the incremental behavior of the assembly. When the initial response is subtracted, the residual ratio $G^{\rm oct}/B - \left(G^{\rm oct}/B\right)_{\rm ini}$ scales with the deviatoric state of the system, by the product $\sigma^*_{\rm dev} F_{\rm dev}$. For

strain amplitudes larger than about 10^{-4}, rearrangements in the sample take place, and the behavior deviates from elastic (reversible). The effect of increasing amplitude of isotropic/deviatoric strain perturbations on isotropic/deviatoric stress and fabric is investigated, in various cases from nearly isotropic states to steady states at various different densities. For very small strain, the initial (linear) elastic regime, visible in the stress response, is associated with strictly no change in fabric. For higher strain amplitude applied to a nearly isotropic state, plasticity comes into play, and the incremental stress–strain relation deviates from linear as soon as the contact network changes. When the system is strained up to the steady state, the elastic regime is tiny (compared to the nearly isotropic states), and both stress and fabric display first elastic and then plastic response to smaller deviatoric strains. In other words, when the system was strained up to the steady state, the elastic regime becomes smaller, and both stress and fabric display no change associated to saturation. Large volumetric strain induces substantial modifications, as the sample previously subjected only to volume-conserving deformation experiences now large volume changes. In the limit of large strain, the tangential moduli of the stress–strain and fabric-strain curves (see Fig. 5) are recovered. The relation between particle rearrangements and macro-scale plasticity is a present object of investigation, as well as the transition between local/global plastic regimes. As an important result, our study provides a new way to indirectly characterize the granular structure. Once the moduli in a given isotropic/anisotropic configuration have been measured by wave propagation experiments, they can be uniquely associated with the internal fabric. However, we do not expect the proportionality factors to remain constant for different materials.

As further step, a simple constitutive model is introduced that involves anisotropy, as proposed in Refs. [48,51]. The nonlinear elastic behavior is established, and the irreversible/ plastic contribution is introduced via empirical probabilities for plastic events, that require more research and theoretical support. The dependence of the model parameters on volume fraction and polydispersity has been analyzed in previous extensive work [30,39]. Here, by using the new relations for the elastic moduli, we are able to integrate the increments at each state along a generic deformation path. Hence, we can predict the evolution of pressure, shear stress and fabric for large strain, and also at and after reversal. The method is first calibrated and then applied to a volume-conserving (undrained) shear cycle. When the prediction is compared with numerical simulations, quantitative agreement is found for the deviatoric field variables. The most notable feature of soft but different response of shear stress and fabric to reversal of strain is well captured; the pressure response amplitude is underestimated by the present model.

This study concerns a seemingly unrealistic material of spheres without friction and interacting with linear contact forces to exclude effects that are due to contact nonlinearity, friction and/or non-sphericity. This allows to unravel the peculiar interplay of stress with microstructure. However, the work should be extended to more realistic cases involving particle shape, friction, and non-linear contact behavior. We expect that friction will not completely change the observed relations between stiffness and fabric state, but possibly will add new effects to be explored in the future; the deviatoric fabric and the moduli are expected to change quantitatively when tangential forces are included. The contacts nonlinearity will introduce an extra pressure-dependence for the moduli, as already shown by many authors (see e.g., [7,16,50,78] in the case of Hertzian interactions). Speculating about the effects of shape goes beyond the scope of this study. A similar analysis is already in progress to check the influence of polydispersity on the relation between elastic stiffness and microstructure, as polydispersity affects the contact network, the structure, and the orientation of contacts [24,25,39].

Future work will focus on the extension of our small perturbation approach to elasto-plasticity, by using concepts like e.g., the Gudehus response envelope [27,54]. Other theoretical approaches involve ideas proposed by Einav [17], or by Jiang and Liu [33], for which our results can provide a microscopically-based calibration of parameters, but details are not discussed here. The information obtained for the pure elastic range can then be used to decouple the plastic contribution, associated with rearrangements, and to study the flow rule. The validation of the present analysis with experimental data is another important goal. Nevertheless, the issue of measuring fabric from laboratory experiments is far from solved, even though big advances have been made in recent years using photoelasticity and microtomography CT-scans [5,29,34,74]. A partial validation is anyway possible when measuring the residual dependence of the elastic response from variables other than stress and porosity [19], by means of acoustic measurements [36]. The behavior after more than one cycle deserves further investigation, from both simulational and theoretical points of view, to detect features like creep, liquefaction and ratcheting, analyzed in preliminary works [51] with constant elastic moduli and for many cycles [41].

Finally, a general tensor formulation that allows for highly different orientations of strain-rate, stress and fabric is an open issue, but can be inspired by the works of Thornton [77] and Zhao and Guo [87].

Acknowledgment We thank Itai Einav (University of Sydney) and Mario Liu (University of Tübingen) for scientific discussions. Critical comments and reviews from O. I. Imole, M. B. Wojtkowski, F. Göncü, J. Ooi and M. Ramaioli are gratefully acknowledged. This work is financially supported by the European Union funded Marie Curie Initial Training Network, FP7 (ITN-238577), see http://www.pardem.eu/ for more information, and by the NWO-STW VICI grant 10828.

References

1. Agnolin, I., Roux, J.-N.: Internal states of model isotropic granular packings. I. Assembling process, geometry, and contact networks. Phys. Rev. E **76**(6, Part 1), 061302 (2007)
2. Alonso-Marroquin, F., Luding, S., Herrmann, H.J., Vardoulakis, I.: Role of anisotropy in the elastoplastic response of a polygonal packing. Phys. Rev. E **71**, 051304 (2005)
3. Bellotti, R., Jamiolkowski, M., Lo Presti, D.C.F., O'Neill, D.A.: Anisotropy of small strain stiffness in Ticino sand. Géotechnique **46**, 115–131 (1996)
4. Belyaeva, I.Y., Zaitsev, V.Y., Ostrovskii, L.A.: Nonlinear acoustoelastic properties of granular media. Acoust. Phys. **39**, 11–15 (1993)
5. Bi, D., Zhang, J., Chakraborty, B., Behringer, R.P.: Jamming by shear. Nature **480**(7377), 355–358 (2011)
6. Calvetti, F., Viggiani, G., Tamagnini, C.: A numerical investigation of the incremental behavior of granular soils. Rivista Italiana di Geotecnica **37**, 11–29 (2003)
7. Chang, C.S.: Micromechanical modeling of deformation and failure for granulates with frictional contacts. Mech. Mater. **16**, 13–24 (1993)
8. Chang, C.S., Chao, S.J., Chang, Y.: Estimates of elastic moduli for granular material with anisotropic random packing structure. Int. J. Solids Struct. **32**, 1989–2009 (1995)
9. Christoffersen, J., Mehrabadi, M.M., Nemat-Nasser: A micro-mechanical description of granular material behavior. J. Appl. Mech. **48**, 339–344 (1981)
10. Chung, C.-K., Jang, E.-R., Baek, S.-H., Jung, Y.-H.: How contact stiffness and density determine stress-dependent elastic moduli: a micromechanics approach. Granul. Matter **16**, 23–39 (2014)
11. Cosserat, F.C.: Théorie des Corps Déformables. Hermann, Paris (1909)
12. Cowin, S.C.: The relationship between the elasticity tensor and the fabric tensor. Mech. Mater. **4**, 137–147 (1985)
13. Dafalias, Y.F., Manzari, M.T.: Simple plasticity sand model accounting for fabric change effects. J. Eng. Mech. **130**, 622–634 (2004)
14. Dagois-Bohy, S., Tighe, B.P., Simon, J., Henkes, S., van Hecke, M.: Soft-sphere packings at finite pressure but unstable to shear. Phys. Rev. Lett. **109**, 095703 (2012)
15. Darve, F., Flavigny, E., Meghachou, M.: Yield surfaces and principle of superposition: revisit through incrementally non-linear constitutive relations. Int. J. Plast. **11**, 927–945 (1995)
16. Digby, P.J.: The effective elastic moduli of porous granular rocks. J. Appl. Mech. **48**, 803–808 (1981)
17. Einav, I.: The unification of hypo-plastic and elasto-plastic theories. Int. J. Solids Struct. **49**, 1305–1315 (2012)
18. Ellenbroek, W.G., van Hecke, M., van Saarloos, W.: Jammed frictionless disks: connecting local and global response. Phys. Rev. E **80**, 061307 (2009)
19. Ezaoui, A., Di Benedetto, H.: Experimental measurements of the global anisotropic elastic behaviour of dry Hostun sand during triaxial tests, and effect of sample preparation. Géotechnique **59**, 621–635 (2009)
20. Farago, O., Kantor, Y.: Fluctuation formalism for elastic constants in hard-spheres-and-tethers systems. Phys. Rev. E **61**, 2478 (2000)
21. Froiio, F., Roux, J.N.: Incremental response of a model granular material by stress probing with DEM simulations. In: Goddard, J., Giovine, P., Jenkins, J.T. (eds.) AIP Conference Proceedings, vol. **1227**, pp. 183–197. Reggio Calabria Italy (2010)
22. Goddard, J.D.: Nonlinear elasticity and pressure-dependent wave speeds in granular media. Proc. R. Soc. Lond. A **430**, 105–131 (1990)
23. Goddard, J.D.: Parametric hypoplasticity as continuum model for granular media: from Stokesium to Mohr–Coulombium and beyond. Granul. Matter **12**, 145–150 (2010)
24. Göncü, F., Durán, O., Luding, S.: Constitutive relations for the isotropic deformation of frictionless packings of polydisperse spheres. C. R. Mécanique **338**, 570–586 (2010)
25. Göncü, F., Luding, S.: Effect of particle friction and polydispersity on the macroscopic stress–strain relations of granular materials. Acta Geotech. **8**, 629–643 (2013)
26. Graham, J., Houlsby, G.T.: Anisotropic elasticity of a natural clay. Géotechnique **33**, 165–180 (1983)
27. Gudehus, G.: A comparison of some constitutive laws for soils under radially symmetric loading and unloading. Canadian Geotechnical Journal **20**, 502–516 (1979)
28. Guo, N., Zhao, J.: The signature of shear-induced anisotropy in granular media. Comput. Geotech. **47**, 1–15 (2013)
29. Hall, S.A., Bornert, M., Desrues, J., Pannier, Y., Lenoir, N., Viggiani, G., Bésuelle, P.: Discrete and continuum analysis of localised deformation in sand using X-ray μCT and volumetric digital image correlation. Géotechnique **60**, 315–322 (2010)
30. Imole, O.I., Kumar, N., Magnanimo, V., Luding, S.: Hydrostatic and shear behavior of frictionless granular assemblies under different deformation conditions. KONA Powder Part. J. **30**, 84–108 (2013)
31. Inagaki, S., Otsuki, M., Sasa, S.: Protocol dependence of mechanical properties in granular systems. Eur. Phys. J. E **34**, 1–6 (2011)

32. Jiang, G.-L., Tatsuoka, F., Koseki, J., Flora, A.: Inherent and stress-state-induced anisotropy in very small strain stiffness of a sandy gravel. Géotechnique **47**, 509–521 (1997)
33. Jiang, Y., Liu, M.: Granular solid hydrodynamics. Granul. Matter **11**, 139–156 (2009)
34. Jorjadze, I., Pontani, L.-L., Brujic, J.: Microscopic approach to the nonlinear elasticity of compressed emulsions. Phys. Rev. Lett. **110**, 048302 (2013)
35. Keim, N.C., Arratia, P.E.: Mechanical and microscopic properties of the reversible plastic regime in a 2D jammed material. Phys. Rev. Lett. **112**, 028302 (2014)
36. Khidas, Y., Jia, X.: Probing the shear-band formation in granular media with sound waves. Phys. Rev. E **85**, 051302 (2012)
37. Krijgsman, D., Luding, S.: 2D cyclic pure shear of granular materials, simulations and model. In: Yu, A., Dong, K., Yang, R., Luding S. (eds.) Powders and Grains 2013, vol. 1542, pp. 1226–1229. AIP Conference Proceedings (2013)
38. Kruyt, N.P., Agnolin, I., Luding, S., Rothenburg, L.: Micromechanical study of elastic moduli of loose granular materials. J. Mech. Phys. Solids **58**, 1286–1301 (2010)
39. Kumar, N., Imole, O.I., Magnanimo, V., Luding, S.: Effect of polydispersity on the micro-macro behavior of granular assemblies under different deformation paths. Particuology **12**, 64–79 (2014)
40. Kumar, N., Imole, O.I., Magnanimo, V., Luding, S.: Evolution of the effective moduli for anisotropic granular materials during shear. In: Yu, A., Dong, K., Yang, R., Luding S. (eds.) Powders and Grains 2013, vol. 1542, pp. 1238–1241. AIP Conference Proceedings (2013)
41. Kumar, N., Luding, S.: Memory of jamming and shear-jamming. In preparation (2014)
42. Kuwano, R., Jardine, R.J.: On the applicability of cross-anisotropic elasticity to granular materials at very small strains. Géotechnique **52**, 727–749 (2002)
43. La Ragione, L., Magnanimo, V.: Contact anisotropy and coordination number for a granular assembly: a comparison of distinct-element-method simulations and theory. Phys. Rev. E. **85** (2012)
44. Lakes, R.: Experimental methods for study of Cosserat elastic solids and other generalized elastic continua. In: Mühlhaus, H. (ed.) Continuum models for materials with micro-structure, pp. 1–25. Wiley, New York (1995)
45. Li, X.S., Dafalias, Y.F.: Constitutive modeling of inherently anisotropic sand behavior. J. Geotech. Geoenviron. Eng. **128**, 868–880 (2002)
46. Li, X.S., Dafalias, Y.F.: Anisotropic critical state theory: role of fabric. J. Eng. Mech. **138**, 263–275 (2012)
47. Luding, S.: Anisotropy in cohesive, frictional granular media. J. Phys. Condens. Matter **17**, S2623–S2640 (2005)
48. Luding, S., Perdahcıoğlu, E.S.: A local constitutive model with anisotropy for various homogeneous 2D biaxial deformation modes. Chemie Ingenieur Technik **83**, 672–688 (2011)
49. Magnanimo, V., La Ragione, L., Jenkins, J.T., Makse, H.A.: Irreversible incremental behavior in granular materials. In preparation (2014)
50. Magnanimo, V., La Ragione, L., Jenkins, J.T., Wang, P., Makse, H.A.: Characterizing the shear and bulk moduli of an idealized granular material. Europhys. Lett. **81**, 34006 (2008)
51. Magnanimo, V., Luding, S.: A local constitutive model with anisotropy for ratcheting under 2D axial-symmetric isobaric deformation. Granul. Matter **13**, 225–232 (2011)
52. Makse, H.A., Johnson, D.L., Schwartz, L.M.: Packing of compressible granular materials. Phys. Rev. Lett. **84**, 4160–4163 (2000)
53. Maugin, G.A., Metrikine, A.V.: Mechanics of generalized continua, vol. 21. Springer, Berlin (2010)
54. Mašín, D.: Asymptotic behaviour of granular materials. Granul. Matter **14**, 759–774 (2012)
55. Métayer, J.F., Suntrup, D.J., Radin, C., Swinney, H.L., Schröter, M.: Shearing of frictional sphere packings. Europhys. Lett. **93**, 64003 (2011)
56. Morgeneyer, M., Schwedes, J.: Investigation of powder properties using alternating strain paths. Task Q. **7**, 571–578 (2003)
57. Muhlhaus, H., Moresi, L., Gross, L., Grotowski, J.: The influence of non-coaxiality on shear banding in viscous-plastic materials. Granul. **12**, 229–238 (2010)
58. Nemat-Nasser, S.: A micromechanically-based constitutive model for frictional deformation of granular materials. J. Mech. Phys. Solids **48**, 1541–1563 (2000)
59. Nicot, F., Darve, F.: Basic features of plastic strains: from micro-mechanics to incrementally nonlinear models. Int. J. Plast. **23**, 1555–1588 (2007)
60. Nicot, F., Darve, F.: Micro-mechanical bases of some salient constitutive features of granular materials. Int. J. Solids Struct. **44**, 7420–7443 (2007)
61. Oda, M.: Initial fabrics and their relations to mechanical properties of granular materials. Soils Found. **1**, 17–36 (1972)
62. O'Hern, C.S., Silbert, L.E., Liu, A.J., Nagel, S.R.: Jamming at zero temperature and zero applied stress: The epitome of disorder. Phys. Rev. E **68**, 011306 (2003)
63. Otsuki, M., Hayakawa, H.: Critical scaling near jamming transition for frictional granular particles. Phys. Rev. E **83**, 051301 (2011)
64. Parisi, G., Zamponi, F.: Mean-field theory of hard sphere glasses and jamming. Rev. Mod. Phys. **82**, 789–845 (2010)
65. Pica Ciamarra, M., Coniglio, A.: Jamming at zero temperature, zero friction, and finite applied shear stress. Phys. Rev. Lett. **103**, 235701 (2009)
66. Röck, M., Morgeneyer, M., Schwedes, J., Kadau, D., Brendel, L., Wolf, D.E.: Steady state flow of cohesive and non-cohesive powders. Granul. Matter **10**, 285–293 (2008)
67. Roscoe, K.H., Schofield, A.N., Wroth, C.P.: On the yielding of soils. Géotechnique **8**, 22–53 (1958)
68. Saitoh, K., Magnanimo, V., Luding, S.: Master equation for the probability distribution functions of overlaps between particles in two dimensional granular packings. http://arXiv:1311.5359 (2014)
69. Satake, M.: Fabric tensor in granular materials. In: Proceedings of IUTAM Symp. on Deformation and Failure of Granular materials. Delft, The Netherlands (1982)
70. Shaebani, M.R., Boberski, J., Wolf, D.E.: Unilateral interactions in granular packings: a model for the anisotropy modulus. Granul. Matter **14**, 265–270 (2012)

71. Shaebani, M.R., Madadi, M., Luding, S., Wolf, D.E.: Influence of polydispersity on micromechanics of granular materials. Phys. Rev. E **85** (2012)
72. Sibille, L., Nicot, F., Donzé, F.-V., Darve, F.: Analysis of failure occurrence from direct simulations. Eur. J. Environ. Civil Eng. **13**, 187–201 (2009)
73. Somfai, E., van Hecke, M., Ellenbroek, W.G., Shundyak, K., van Saarloos, W.: Critical and noncritical jamming of frictional grains. Phys. Rev. E **75**, 020301 (2007)
74. Sperl, M.: Experiments on corn pressure in silo cells. Translation and comment of Janssen's paper from 1895. Granul. Matter **8**, 59–65 (2006)
75. Sun, J., Sundaresan, S.: A constitutive model with microstructure evolution for flow of rate-independent granular materials. J. Fluid Mech. **682**, 590–616 (2011)
76. Tejchman, J., Bauer, E., Wu, W.: Effect of fabric anisotropy on shear localization in sand during plane strain compression. Acta Mech. **189**, 23–51 (2007)
77. Thornton, C.: Quasi-static simulations of compact polydisperse particle systems. Particuology **8**, 119–126 (2010)
78. Walton, K.: The effective elastic moduli of a random packing of spheres. J. Mech. Phys. Solids **35**, 213–226 (1987)
79. Wang, X., Zhu, H.P., Luding, S., Yu, A.B.: Regime transitions of granular flow in a shear cell: A micromechanical study. Phys. Rev. E **88**, 032203 (2013)
80. Wang, Y.H., Mok, C.M.: Mechanisms of small-strain shear-modulus anisotropy in soils. J. Geotech. Geoenviron. Eng. **134**, 1516–1530 (2008)
81. Wu, W.: Rational approach to anisotropy of sand. Int. J. Numer. Anal. Methods Geomech. **22**, 921–940 (1998)
82. Yang, Z.X., Li, X.S., Yang, J.: Quantifying and modelling fabric anisotropy of granular. Géotechnique **58**, 237–248 (2008)
83. Yimsiri, S., Soga, K.: DEM analysis of soil fabric effects on behaviour of sand. Géotechnique **60**, 483–495 (2010)
84. Yoshimine, M., Ishihara, K., Vargas, W.: Effects of principal stress direction and intermediate principal stress on undrained shear behavior of sand. Soils Found. **38**, 179–188 (1998)
85. Zhang, H.P., Makse, H.A.: Jamming transition in emulsions and granular materials. Phys. Rev. E **72**, 011301 (2005)
86. Zhang, J., Majmudar, T., Tordesillas, A., Behringer, R.: Statistical properties of a 2D granular material subjected to cyclic shear. Granul. Matter **12**, 159–172 (2010)
87. Zhao, J., Guo, N.s: Unique critical state characteristics in granular media considering fabric anisotropy. Géotechnique **63**, 695–704 (2013)